Structure of the crust in the vicinity of the Banggong-Nujiang suture in central Tibet from INDEPTH magnetotelluric data

Kurt D. Solon,[1,2] Alan G. Jones,[3,4] K. Douglas Nelson,[1,5] Martyn J. Unsworth,[6] William F. Kidd,[7] W. Wei,[8] H. Tan,[8] S. Jin,[8] M. Deng,[8] J. R. Booker,[9] S. Li,[9] and P. Bedrosian[9,10]

Received 16 January 2003; revised 31 March 2005; accepted 8 June 2005; published 11 October 2005.

[1] Magnetotelluric data from a 150-km-long profile crossing the Banggong-Nujiang suture (BNS), central Tibet, acquired as part of the International Deep Profiling of Tibet and the Himalaya (INDEPTH) project, have been examined for crustal and upper mantle structure. Strike and dimensionality analyses demonstrate that regional-scale electrical structures are two-dimensional and oriented approximately parallel to surface geological strike. As seen elsewhere in Tibet, the double thickness crust is generally characterized by resistive upper crust (hundreds to thousands of ohm meters) overlying conductive middle and lower crust (tens to hundreds of ohm meters), but in detail, there are lateral variations at all levels. Regionally, a northward transition from thick (~45 km) to thin (~15 km) resistive upper crust coincides with (1) the surface trace of the BNS, (2) a prominent strand of the Karakorum-Jiali fault system, (3) northward decrease in upper mantle seismic velocities and increase in attenuation, and (4) pronounced northward onset of seismic polarization anisotropy. The latter two seismological features have been taken to mark the northern limit of Indian mantle lithosphere thrust beneath southern Tibet. On the basis of our electrical model, we speculate that (1) the resistive upper crustal root beneath the Neogene Lunpola and Duba basins was produced by crustal shortening localized along the northern edge of the Lhasa terrane; (2) the low midcrustal resistivity beneath the BNS reflects enhanced Neogene melting and/or metamorphic dewatering of relatively fertile subduction zone complex rocks; (3) observed steep upper crustal low-resistivity anomalies are produced by hydrothermal fluids within active faults localized within and adjacent to the BNS; and (4) these strike-slip and extensional fault arrays are surface manifestations of lithosphere-penetrating shear localized along the northern edge of the underthrust Indian plate.

Citation: Solon, K. D., et al. (2005), Structure of the crust in the vicinity of the Banggong-Nujiang suture in central Tibet from INDEPTH magnetotelluric data, *J. Geophys. Res.*, *110*, B10102, doi:10.1029/2003JB002405.

1. Introduction

[2] The Himalaya and adjacent Tibetan Plateau together compose the type example of an active continent-continent collision zone and are a benchmark for the study of ancient collisional orogens. The plateau stands, on average, 5 km above sea level and represents the largest expanse of thickened continental crust on Earth. Thickening of the plateau crust is a consequence of the collision between India and Asia [e.g., *Argand*, 1924; *Dewey and Burke*, 1973; *Molnar*, 1988; *Tapponnier et al.*, 2001], which began ~50 Myr ago [*Rowley*, 1996] (although this is debated and thought by some to be much older [*Yin and Harrison*, 2000]) and continues to the present. Since 1991, scientists working under the auspices of Project International Deep Profiling of Tibet and the Himalaya (INDEPTH) have acquired geophysical and geological data on the plateau with the goal of elucidating the structure of the crust and mantle lithosphere beneath this region [*Zhao et al.*, 1993; *Nelson et al.*, 1996]. Three field campaigns, INDEPTH I, II, and III, have been completed to date, during which geophysical and geological data have been acquired along a series of north-south trending profiles. The total INDEPTH lines now compose a discontinuous transect extending from the crest of the Himalaya to the northern interior of the

[1]Department of Earth Sciences, Syracuse University, Syracuse, New York, USA.
[2]Now at Exxon Mobil, Exploration Company, Houston, Texas, USA.
[3]Geological Survey of Canada, Ottawa, Ontario, Canada.
[4]Now at Dublin Institute for Advanced Studies, Dublin, Ireland.
[5]Deceased 17 August 2002.
[6]Department of Physics, Avadh Bhatia Physics Laboratory, University of Alberta, Edmonton, Alberta, Canada.
[7]Department of Earth and Atmospheric Sciences, State University of New York, Albany, New York, USA.
[8]China University of Geosciences, Beijing, China.
[9]Department of Earth and Space Sciences, University of Washington, Seattle, Washington, USA.
[10]Now at U.S. Geological Survey, Denver, Colorado, USA.

0148-0227/05/2003JB002405$09.00

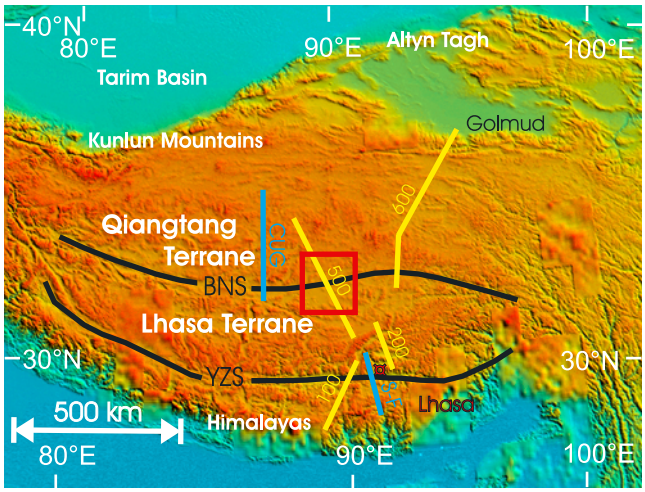

Figure 1. Digital elevation model of the Tibetan Plateau produced from data described by *Fielding et al.* [1994]. INDEPTH magnetotelluric profiles shown in yellow. Numbers (100, 200, 500, 600) represent the name of each INDEPTH MT line. Blue lines illustrate general area of previous MT surveys (SF, Sino-French survey; CUG, China University of Geosciences survey). Region of study of the BNS zone is outlined in red box. YZS, Yarlung-Zangbo suture; BNS, Banggong-Nujiang suture.

plateau (Figure 1). Electromagnetic acquisition, using the natural source magnetotelluric (MT) technique, was added during INDEPTH II and III. Both broadband and long-period MT data were recorded to determine the electrical resistivity structure of the Tibetan Plateau crust and uppermost mantle, and to complement the geological and seismological studies.

[3] During INDEPTH III, a 500-km-long MT profile was collected extending from the center of the Lhasa terrane to the center of the Qiangtang terrane in central Tibet (Figure 1). This profile, termed the 500 line by *Wei et al.* [2001], crosses the Late Jurassic–Early Cretaceous Banggong-Nujiang suture zone (BNS) which separates the two terranes, as well as a roughly coincident first-order south-to-north change in the seismological properties of the Tibetan Plateau (discussed below). *Wei et al.* [2001] have summarized the plateau-scale electrical structure observed using the data on this profile together with the other INDEPTH profiles shown in Figure 1 (yellow lines). In this paper, we present a substantially more detailed analysis of a subset of those data from the sites crossing the BNS. We compare our best fit electrical resistivity model with seismic and surface geological data for the region and demonstrate spatial correlations that give insight into both the structure and physical properties of the crust in this key region of the Tibetan Plateau.

2. Banggong-Nujiang Suture: Geological Setting

[4] The Banggong-Nujiang suture (BNS) trends approximately east-west across the interior of the Tibetan Plateau (Figure 1). It formed in Late Jurassic–Early Cretaceous times when the Lhasa terrane collided with the southern margin of Asia (Qiangtang terrane) to the north [*Girardeau et al.*, 1984; *Dewey et al.*, 1988; *Taylor et al.*, 2003]. The BNS is defined geologically by the northern limit of scattered ophiolite fragments which were thrust southward over middle Jurassic flysch of the Lhasa terrane [*Girardeau et al.*, 1984]. *Girardeau et al.* [1984] suggested that these ophiolite fragments are erosional remnants of a once continuous ophiolite sheet. The interpreted southward obduction of this ophiolite sequence implies a northward paleosubduction polarity of the Lhasa terrane beneath the Qiangtang terrane [*Girardeau et al.*, 1984; *Pearce and Deng*, 1988; *Kidd et al.*, 1988; *Dewey et al.*, 1988].

[5] Stratigraphy and facies of pre-BNS strata of both the Lhasa terrane and the Qiangtang terrane are largely marine clastics and carbonates in successions several kilometers thick [*Leeder et al.*, 1988], which imply that they were deposited over continental crust, likely stretched significantly by rifting and formation of passive continental margins [e.g., *Leeder et al.*, 1988]. The Lhasa terrane has a Gondwanan origin; the Qiangtang is Gondwanan in the west [*Norin*, 1946], but Cathasian in the east, which led *Kidd et al.* [1988] to suggest that the ophiolite and blueschist occurrences [*Hennig*, 1915] within the central Qiangtang represent an internal suture predating the BNS. *Kapp et al.* [2000] provide the alternative interpretation that in late Triassic time, during closure of the Paleo-Tethys, the Triassic age Songpan-Ganzi flysch complex was subducted beneath the Qiangtang terrane. In early Jurassic time low-angle normal faults subsequently exhumed the underplated flysch complex from middle and lower crustal levels to the surface.

[6] Subsequent to BNS ophiolite obduction, a substantial early mid-Cretaceous granitoid batholithic belt was developed in the northern Lhasa terrane (Baingoin granites [*Harris et al.*, 1988]), identified as collisional magmatism by *Harris et al.* [1990]. Widespread mid-Cretaceous limestones give evidence of normal crustal thickness at the time of their deposition [*Dewey et al.*, 1988]. Significant thrust and fold shortening of the Lhasa terrane sedimentary section, including these limestones, occurred in the region of the MT profile after the mid-Cretaceous. It is inferred that most of this shortening in the southern and western parts of the Lhasa terrane occurred prior to the Paleocene [*Burg et al.*, 1983; *Murphy et al.*, 1997; *Pan and Kidd*, 1999], although some Cenozoic shortening occurs in those regions, and this could have been more significant in the area of the MT line discussed here.

[7] The present crustal thickness of central Tibet is about 65 km; it is unclear how much thickening was produced during the BNS collision, or during subsequent shortening episodes, and whether any thickening persisted up to the time of the initiation of the Tertiary India-Asia collision [*Kidd and Molnar*, 1988; *Murphy et al.*, 1997; *Yin and Harrison*, 2000]. The BNS has been overprinted by Tertiary transpressional tectonics, as is evident by the existence of a zone of thrust and transpressional faults cutting Tertiary sediments deposited on and immediately adjacent to the BNS [*Coward et al.*, 1988; *Kidd et al.*, 1988; *Kidd and Molnar*, 1988; *Kapp et al.*, 1998, 1999; *Yin and Harrison*, 2000; *Taylor et al.*, 2001, 2002, 2003]. Yin and his students [*Kapp et al.*, 1998; *Yin and Harrison*, 2000] have claimed that there may be a surprisingly large

amount of Cenozoic shortening represented in these structures [~200 km], although this is not unambiguously demonstrated.

[8] Some of the youngest faults in this zone are late Neogene or active Recent structures. They belong to a more widespread fault array that extends east-west across the interior of the Tibetan Plateau, the most prominent members of which are right-lateral strike-slip faults of what has been termed the Karakorum-Jiali fault system [*Armijo et al.*, 1986, 1989]. *Taylor et al.* [2001, 2002, 2003] have recently presented evidence that the left-lateral faults, typically located at and north of the BNS, accommodate a comparable rate of strain to the right-lateral faults of the Karakorum-Jiali system emphasized by *Armijo et al.* [1989].

[9] The central and western Tibetan Plateau is currently undergoing east-west extension, manifest by widely distributed north trending normal faults and rifts, and both ENE (left-lateral) and WNW (right-lateral) trending strike-slip transfer faults [*Tapponnier et al.*, 1981; *Armijo et al.*, 1986, 1989; *Pan and Kidd*, 1992; *Harrison et al.*, 1995; *Yin et al.*, 1999; *Yin*, 2000; *Yin and Harrison*, 2000; *Taylor et al.*, 2003]. Studies of three fault sets adjacent to the BNS separated by 400 km and 70 km in central Tibet reveal conjugate strike-slip faults across the BNS with NE striking left slip faults north of the BNS and NW striking right-slip faults south of the BNS [*Taylor et al.*, 2003]. These extensional structures locally provide conduits for geothermal fluids, as evidenced by the presence of hot springs found along the faults. Although the density of hot springs decreases northward across the plateau [*Hochstein and Regenauer-Lieb*, 1998], several are coincident with the INDEPTH III profile in central Tibet. Of relevance to this study is a geothermal spring found at the edge of Lake Doima, located ~20 km north of the mapped position of the BNS, near 89°E (see below).

[10] Also significant are small occurrences of volcanics, probably Neogene in age but not yet isotopically dated, which occur on the line of the profile where it crosses the BNS and about 100 km north of this point (about 30 km north of the end of the part of the profile considered in this paper). More extensive Cenozoic volcanics occur yet farther north, east of the end of the MT 500 line and beyond; these are dated mostly 8–10 Ma [*Turner et al.*, 1993].

[11] The BNS also coincides regionally with major south-to-north changes in the seismic properties of the Tibetan lithosphere. These include a modest northward thinning of the plateau crust [*Molnar*, 1988; *Zhao et al.*, 2001], a substantial northward decrease in both *P* and *S* wave velocities and increase in attenuation of the underlying uppermost mantle [*Ni and Barazangi*, 1983; *Molnar*, 1988; *Owens and Zandt*, 1997], and abrupt northward onset of seismic polarization anisotropy [*Huang et al.*, 2000] (see below), a change in upper mantle velocities with lower velocities to the north [*Meissner et al.*, 2004], and a change in receive functions [*Kind et al.*, 2002]. These coincident south-to-north changes have been interpreted by a number of investigators to mark the northern limit of relatively old, cold Indian mantle lithosphere thrust beneath Tibet during Tertiary time (summarized by *Owens and Zandt* [1997]). There are also crustal differences on either side of the BNS, with seismically faster crust to the south compared to the north [*Mechie et al.*, 2004; *Meissner et al.*, 2004].

3. Magnetotelluric Method and Prior Tibetan MT Experiments

3.1. Magnetotelluric Method

[12] The magnetotelluric (MT) method utilizes naturally occurring time-varying electromagnetic (EM) fields, measurable at the Earth's surface, to investigate the distribution of electrical resistivity (inverse of conductivity) in the subsurface [e.g., *Vozoff*, 1986, 1991; *Jones*, 1992, 1998, 1999; *Jiracek et al.*, 1995]. Natural sources of EM fields are lightning activity at short periods (<1 s), and interactions of solar plasma ejecta with the Earth's magnetosphere at long periods (>1 s). These EM fields propagate globally within the Earth-ionosphere waveguide, and are partially reflected downward into the Earth generating secondary fields within electrically conductive material. Electrical conductivity enhancement within the Earth's lithosphere is caused dominantly by electrolytic conduction through saline aqueous fluids (brines) in interconnected rock fractures and pores, electrolytic conduction through a melt phase, and solid state conduction through interconnected conductive minerals (e.g., graphite, ilmenite, pyrrhotite); or a combination of the above [*Jones*, 1992; *Duba et al.*, 1994].

[13] In the MT method, time series recordings of two orthogonal horizontal components of the time-varying electric field (e_x, e_y), and three orthogonal components of the time-varying magnetic field (h_x, h_y, h_z) are made at each site [e.g., *Vozoff*, 1972, 1986, 1991]. In the frequency domain the horizontal electric and magnetic field components are related to each other by the 2×2 complex magnetotelluric impedance tensor, and the vertical magnetic component is related to the horizontal magnetic components by the 1×2 complex geomagnetic transfer function (TF).

[14] The MT impedance tensor contains information about the subsurface beneath the site, and can be analyzed for dimensionality and strike directionality. If the subsurface is characterized by dominantly two-dimensional (2-D) resistivity structures, then the MT impedance tensor in the strike direction becomes antidiagonal. Thus the 2-D geoelectric strike direction can be obtained from appropriate analysis of the tensor [e.g., *Jones and Groom*, 1993; *McNeice and Jones*, 2001]. In two dimensions, Maxwell's equations devolve into two independent sets of equations, one involving current flowing along the 2-D structures, called the transverse electric (TE) mode, and the other involving current flow across the structures, the transverse magnetic (TM) mode. The tensor estimates from either or both modes can be modeled, using forward trial-and-error modeling and/or objective iterative inversion, to determine the subsurface resistivity distribution.

[15] MT studies have proven particularly informative in tectonically active regions where fluids and/or melt are present within the lithosphere [e.g., *Martinez-Garcia*, 1992; *Jones and Dumas*, 1993; *Jiracek et al.*, 1995; *Wannamaker et al.*, 1997a, 1997b; *Jones*, 1998; *Partzsch et al.*, 2000; *Ledo and Jones*, 2001] because the presence of an interconnected melt or brine increases the bulk conductivity (decreases the resistivity) of the host rock by several orders of magnitude. For example, the laboratory measured resistivity value of

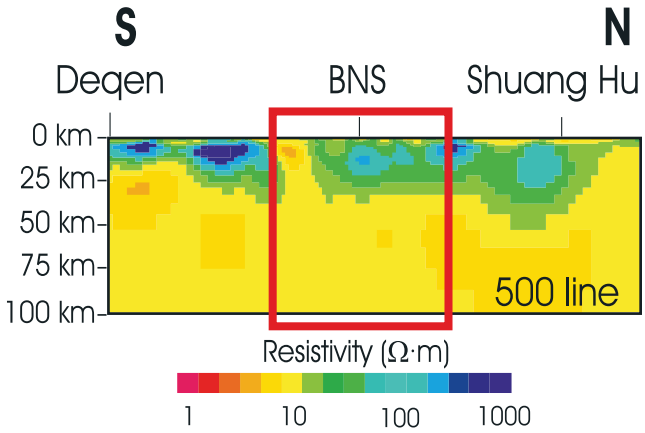

Figure 2. Section around the BNS from the regional-scale resistivity model of *Wei et al.* [2001]. This model was derived from modeling the TM mode MT data only. The red box indicates the region of this study.

dry granite at 500°C is ~100,000 Ω m, but drops by 5 orders of magnitude when a saline fluid is added [*Olhoeft*, 1981; *Shankland and Ander*, 1983]. A similarly large effect, of 2–3 orders of magnitude, is produced by the presence of an interconnected melt [e.g., *Partzsch et al.*, 2000]. Studies demonstrate that even at low orders of partial melt (<1%), the melt phase can connect very effectively [*Minarik and Watson*, 1995], consistent with studies of two-phase analogues of initiation of melt [*Watanabe and Kurita*, 1993].

[16] In Tibet, MT studies have shown that resistivity values range from as high as 10,000 Ω m in the upper crust to locally as low as 1 Ω m in the middle crust [*Chen et al.*, 1996]. These observations have catalyzed an ongoing debate concerning the distribution, amount, and types of fluids that may be present in the Tibetan crust [e.g., *Nelson et al.*, 1996; *Makovsky and Klemperer*, 1999; *Alsdorf and Nelson*, 1999; *Partzsch et al.*, 2000; *Li et al.*, 2003].

[17] MT studies have also proven useful in delineating ancient sutures, for example in the Mesozoic Talkeetna-Alaskan orogen [*Stanley et al.*, 1990] and the Paleoproterozoic Trans-Hudson orogen of North America [*Jones*, 1993a; *Jones et al.*, 1993, 2005]. Suggested causes of decreased resistivity associated with suture zones include graphitic metapelites [*Stanley et al.*, 1990], disseminated sulfide mineralization [*Jones*, 1993a; *Jones et al.*, 1997], and interconnected graphite [e.g., *Camfield and Gough*, 1977; *Pous et al.*, 2004; *Evans et al.*, 2005].

[18] MT studies have also proven useful in delineating the subsurface geometry of major strike-slip faults systems. The faults are evident due to the presence of aqueous fluids within the fault zone, or a change of resistivity across the fault [e.g., *Jones et al.*, 1992; *Unsworth et al.*, 1997; *Ledo et al.*, 2002; *Wu et al.*, 2002; *Ritter et al.*, 2003].

3.2. Previous Magnetotelluric Investigations in Tibet

[19] The first MT survey in Tibet was undertaken by a Sino-French group in the early 1980s [*van Ngoc et al.*, 1986]. Data were collected in the southern part of the Tibetan Plateau along a 200-km north trending profile crossing the Yarlung-Zangbo suture (YZS) at longitude ~90° East (Figure 1). The YZS marks the surface expression of the closure of the Neo-Tethys Ocean that lay between India and Asia prior to the Himalayan collision. The MT responses indicated anomalously low resistivity in the upper to middle crust beneath the profile. This result, taken together with the observation of high heat flow measured in lakes in southern Tibet [*Francheteau et al.*, 1984], led *van Ngoc et al.* [1986] to suggest that zones of partial melt are present at shallow depths within the southern Tibetan crust.

[20] During the early 1990s the China University of Geosciences in Wuhan collected MT data along a north trending profile spanning the Qiangtang terrane in north central Tibet [*Zhang et al.*, 1996] (Figure 1). This study suggested the existence of multiple low-resistivity (1–50 Ω m) layers within the southern Qiangtang crust, but only one such layer beneath the northern part of the terrane.

[21] Both of these previous surveys used state-of-the-art methods for their time, but recorded limited bandwidth data at widely spaced sites, and used what are now regarded as obsolete processing, analysis, and modeling techniques. Nevertheless, these surveys provided the first evidence of anomalously conductive material within the crust of Tibet.

4. INDEPTH MT Surveys: Regional Observations

[22] Modern wide-bandwidth MT investigation of the plateau's lithospheric structure began in 1995 with the advent of the INDEPTH MT surveys [*Chen et al.*, 1996]. To date, INDEPTH has collected ~1500 km of closely spaced broadband MT data along five lines that, taken together, span the plateau (Figure 1). *Wei et al.* [2001] presented a first-order characterization of the electrical structure of the plateau by performing a two-dimensional (2-D) minimum structure inversion (using the RLM2DI code of *Rodi and Mackie* [2001]) of the responses from the entire suite of INDEPTH MT profiles derived from the transverse magnetic (TM) mode data alone [*Wei et al.*, 2001], and recently *Unsworth et al.* [2004] presented models from the 600 line profile lying some 200 km to the east of the study area (Figure 1), with sparse coverage of the BNS. The inversions of *Wei et al.* [2001] portray the general feature of the plateau's resistivity structure. However, because the transverse electric (TE) and the vertical field transfer function (TF) data were not included, they are not appropriate for investigating detailed structure [*Jones*, 1993b]. In particular, the TM mode data alone will not image narrow steep conductors, and tends to overestimate the amount of conducting material present. The TE mode data are more sensitive to narrow subvertical conductive zones, to the conductivity-thickness product of a conductive zone, and to the depth to those zones [*Wannamaker et al.*, 1984; *Agarwal et al.*, 1993].

[23] The model of *Wei et al.* [2001] from the whole 500 line is shown in Figure 2, with the study area of this work in the red box. Although more detailed analyses of these data are ongoing, several first-order features are unlikely to change as a consequence of more refined analysis and modeling. Principal among these is the observation that the middle crust of Tibet (depths of 20–40 km) is electrically conductive across the entire north-south

extent of the plateau, i.e., order of magnitudes more conductive than dry lower crustal rocks at these pressure-temperature conditions [*Kariya and Shankland*, 1983; *Fuji-ta et al.*, 2004]. In general, the depth to the top of the low-resistivity middle crust appears to increase, and the total conductance of the crust decrease, from south to north.

[24] Several local zones of extremely low resistivity are observed in both southern and northern Tibet. The former coincide spatially with bright spot reflections imaged on INDEPTH II seismic reflection profiles [*Chen et al.*, 1996; *Brown et al.*, 1996], which have been interpreted as ponded melt [*Nelson et al.*, 1996] or brine [*Makovsky and Klemperer*, 1999] trapped within the Tibetan crust. The northern structures occur along strike of Pliocene to Recent volcanics found in northern Tibet [*Turner et al.*, 1993].

5. INDEPTH MT Data Acquisition, Analysis, and Corrections

5.1. Data Acquisition

[25] The MT data analyzed for this study are a subset of the INDEPTH III 500 line. This NNW trending profile extends ~400 km from Nam Tso, in the central Lhasa terrane, to Longwei Tso, in the center of the Qiangtang terrane, crossing the BNS near 89.5°E (Figures 1 and 3). The data were acquired in 1998 with two EMI MT-24 broadband (0.004 s to ~50 s) recording systems, used for shallow to midcrustal data acquisition (BBMT), and 15 Phoenix Geophysics LRMT instruments, for long-period (~50 s to ~15,000 s), deep crustal/upper mantle data (LMT). The latter are commercial clones of the Geological Survey of Canada's LiMS systems [*Andersen et al.*, 1988] utilizing a ring core magnetometer [*Narod and Bennest*, 1990]. On the whole profile, the LMT data were recorded at 26 approximately evenly spaced stations (~15 km separation), with BBMT data at 56 stations (~7 km spacing) in between, and coincident with, each of the LMT sites. Solar activity was at adequate to good levels throughout most of the survey. The collocated BBMT and LMT sites used the same layout configuration as closely as possible, with the important exception that the BBMT used a three-electrode L array compared to the LMT five-electrode X array (includes one electrode in the center); this required a compensation factor to be applied to the LMT apparent resistivity data (see below). For this study, we used 21 BBMT sites of the total 56-site set, nine of which had collocated LMT recording (Figure 3), chosen to image optimally the BNS.

5.2. Data Processing

[26] The BBMT time series were processed using the algorithm of *Egbert* [1997] without remote referencing (due to timing problems). The LMT time series were processed using remote references in order to reduce autopower bias errors (i.e., local magnetic noise) [*Gamble et al.*, 1979]. They were processed using a robust, multiremote, variance-minimization extension of the method described by *Jones and Jödicke* [1984] (method 6 of *Jones et al.* [1989]). Both data yielded MT response estimates (impedance tensors), expressed as apparent resistivities (ρ_a) and phases (ϕ), for each site. At the nine coincident sites the BBMT and LMT data were merged to obtain estimates covering more than seven decades in period (0.004 s to 14,285 s). Because of the differences in electrode layout described above, the BBMT and LMT apparent resistivity curves were not typically consistent in the overlap decade of 10–100 s, although the phase responses were. This is a classic example of static shifts problems [*Jones*, 1988]. To merge these data we derived the multiplicative factors required to coalesce the apparent resistivity curves, and applied these factors to the LMT apparent resistivities.

5.3. Distortion Analysis and Correction

[27] In order to obtain a valid regional electrical resistivity model, prior knowledge of the inherent dimensionality (1-D, 2-D, or 3-D) and directionality (geoelectric strike direction) information, and their variation with increasing period (depth penetration), in the MT data are required. Small outcropping or near-surface zones of anomalously low or high resistivity, which are not important geologically, can distort the MT impedance tensors, with the consequence that the tensor estimates do not accurately reflect regional structures. The critical first step therefore is to examine the data quantitatively and determine the extent to which the data fit dimensionality assumptions before any interpretation of the data can be made. If the data can be validly interpreted as representative of 2-D regional structures, then, to correct for galvanic distortions, the observed impedance tensor estimates are fit statistically to a model that includes galvanic distortion of electric fields, the regional 2-D impedances, and the geoelectric strike of the 2-D structure(s).

[28] Following the methods of *Groom and Bailey* [1989] and *Groom et al.* [1993], as extended by *McNeice and Jones* [2001], distortion models were fit to the MT response estimates, in single-site, single-frequency and in multisite, multifrequency modes, to evaluate the structural dimensionality of the data and to determine the dominant crustal geoelectric strike direction. The unconstrained Groom-Bailey (GB) strike directions for each of the 21 sites, calculated in the four period bands, 0.1–1 s, 1–10 s, 10–100 s, and 100–1000 s are shown in Figure 4. An impedance noise floor of 1.75% (equivalent to 3.5% in apparent resistivity and 1° in phase) was set for distortion model fitting. The azimuth of the arrows is the preferred geoelectric strike direction for that period band, and the length of the arrow is an indicator of how well the data fit the assumed distortion model. Long arrows represent a good fit (root mean square misfit <2), while short arrows suggest a poor fit (or no preference) between the data and the model. Misfit could be a consequence of 3-D electrical structure or parametric error estimates that are overly optimistic [*Chave and Jones*, 1997].

[29] Although the sites have variable misfit and strike direction over the four period bands, the predominant strike direction for all periods sensing the crust (periods <1,000 s) is period-independent and lies between N85°E and N100°E. This overall E-W strike direction is consistent with the regional strike of exposed bedding [*Kidd et al.*, 1988], and the general trend of the BNS. This suggests that a 2-D description of the regional resistivity structure(s) is valid and appropriate. Following this assumption, the analyzed period bands were compared in order to retrieve a consistent regional strike estimate for all periods at all sites in our

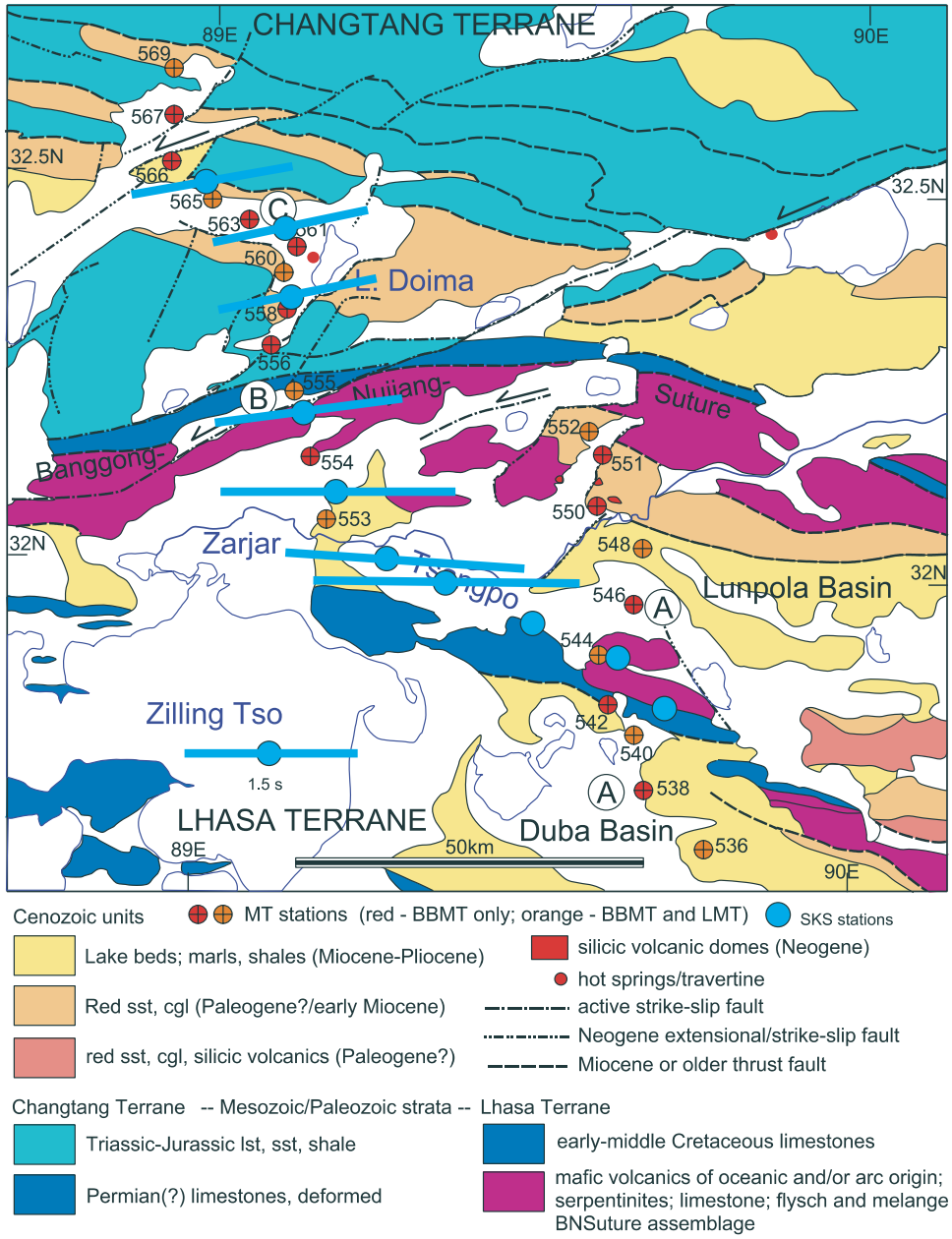

Figure 3. Geological map of the region around the BNS from W. S. F. Kidd (unpublished map, 2003). Twenty-six (of 56 total) INDEPTH III MT stations shown with colored dots. Red dots represent BBMT station locations, and orange dots show sites where both BBMT and LMT data were recorded. Blue dots represent teleseismic stations, and the lines give the *SKS* time delay and fast direction [from *Huang et al.*, 2000]. Letters indicate location of model features described in text.

defined subset. Results of this analysis show that the bulk of the crust beneath this region has a preferred electrical strike direction of 095°. The entire subset was then corrected for distortion, i.e., the regional impedances were determined by fitting the impedance estimates to a distortion model with fixed azimuth (095°). Note this is not equivalent to rotating the estimates into the derived geoelectric strike direction [*Jones and Groom*, 1993; *McNeice and Jones*, 2001]. Where galvanic distortion was high, i.e., large values of Groom-Bailey twist and shear, there were significant differences between the estimated distortion-corrected impedances and the rotated impedances.

[30] In the resulting coordinate system, the transverse electric (TE) mode data represent the response for currents flowing parallel to the geoelectric strike direction (095°) and the transverse magnetic (TM) mode data represent the response for current flowing perpendicular to strike (005°).

5.4. Anisotropy and Site Gain Correction

[31] Once the MT responses have been tensor decomposed into the correct regional coordinate system, there remain two unresolved amplitude-scaling effects; anisotropy (s) and site gain (g). These static shift factors displace the apparent resistivity curves up or down by a frequency-

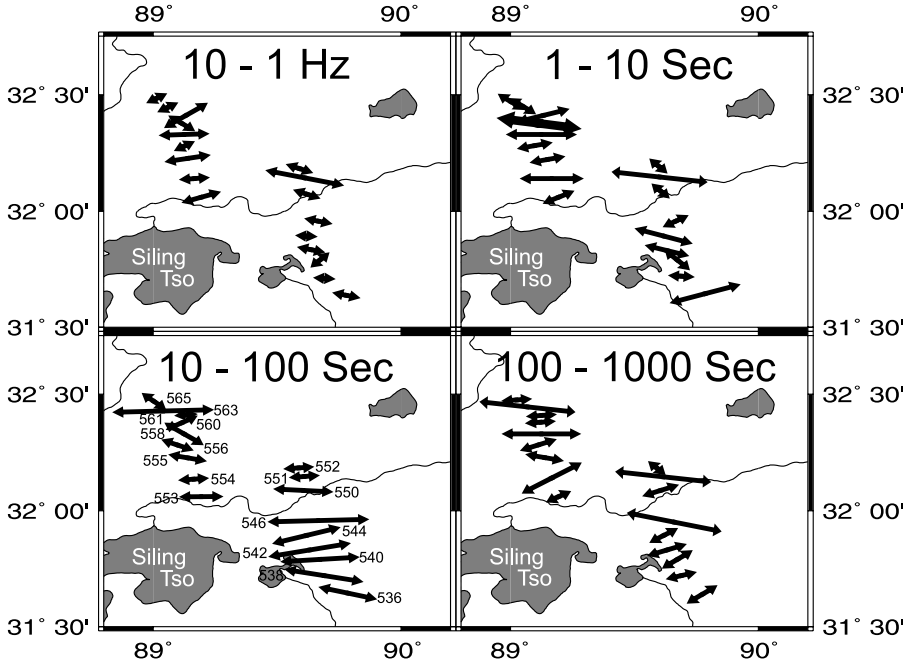

Figure 4. Unconstrained Groom-Bailey strike directions for four period bands. The azimuth of the arrows is the preferred geoelectric strike direction for that decade. The length of the arrow is an indicator of how well the data fit the assumed distortion model. Long arrows represent a good fit. Short arrows suggest a large misfit (or no preference) between the data and the model. Site numbers are illustrated in the 10–100 s plate.

independent constant but leave the phase curves unaffected [e.g., *Jones*, 1988; *Sternberg et al.*, 1988; *Jiracek*, 1990]. These static shifts need to be accounted for in order to minimize errors in the resistivity levels and to give correct depth estimates in the inversion process [e.g., *Groom and Bailey*, 1989]. The anisotropy, also called curve splitting, at each site was removed by coalescing the short-period asymptotes (at ~0.005 s) of the TE and TM mode apparent resistivity curves at each site to their geometric means.

[32] Analysis of the anisotropy-corrected apparent resistivity curves shows only minor amplitude variance due to local site gain, in accordance with *Groom and Bailey*'s [1989] synthetic modeling but which is not always true [e.g., *Marquis et al.*, 1995]. This variation was too small to indicate whether the amplitude shifts were due to site gain effects or real electrical structure. The final apparent resistivity amplitudes were constrained using two different inversion strategies. In the first, no site gain corrections were applied to the data when using *Rodi and Mackie*'s [2001] RLM2DI algorithm. However, when using the RRI algorithm of *Smith and Booker* [1991], with the modifications of *Wu et al.* [1993], the site gain factors from all sites were allowed to vary in order to produce the smoothest model that fits the data. The first-order features described below were the same in both final models, indicating that most of the variation in the resistivity amplitudes is due to the electrical structure of the crust and not to local static effects.

5.5. Regional Phase Responses

[33] The dominant lateral variation of resistivity along an MT profile can be inferred qualitatively from phase versus period contoured pseudosection plots. Unlike apparent resistivities, phases are not affected by galvanic static effects [*Jones*, 1988]. For a homogeneous half-space the phase angle between the electric and magnetic fields is 45°. Exactly for a 1-D Earth and generally for a 2-D or 3-D Earth, phases greater than 45° indicate a transition to less resistive material with depth, and conversely phases less than 45° indicate an increase in resistivity with depth.

[34] The TM and TE mode data for the distortion-corrected phase responses are contoured in pseudosection form in Figure 5 (first, and third panels in Figures 5 (right) and 5 (left)). Period is plotted along the ordinate on a logarithmic scale in order to approximate the exponential decay of EM field amplitudes with depth. Light green and yellow suggest areas of increasing resistivity with depth; conversely, dark green and blues suggest zones of decreasing resistivity with depth. The major features evident in Figure 5 are that (1) there is local variability along the whole profile in the very short period (<0.1 s) phases of both modes, which indicates shallow along-profile lateral variations in resistivity and is likely the result of local, near-surface geological structures, such as conductive sedimentary basins juxtaposed against resistive crystalline basement; (2) in general, periods <10 s are characterized by phases <45°, which suggests a generally resistive uppermost crust; and (3) in contrast, phases at periods >10 s are >45° in both modes at nearly all sites. This is a strong indication that resistivity decreases with depth beneath the entire profile.

6. Data Inversion

6.1. The 500 Line Resistivity Model Inversion

[35] The corrected MT responses were modeled with two different inversion algorithms using numerous different

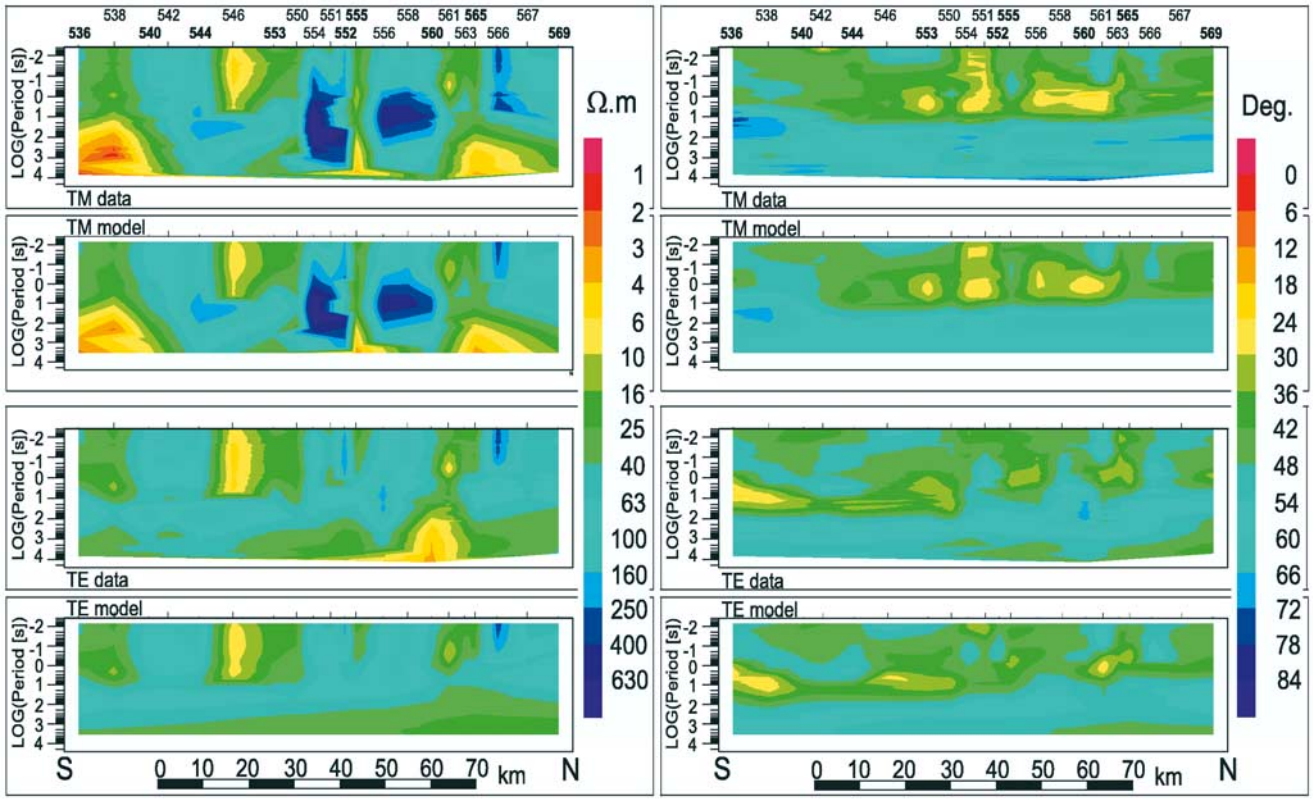

Figure 5. Pseudosections illustrating (left) the measured apparent resistivities and (right) phases and the RLM2DI theoretical responses for both the TM and TE modes of data. BBMT plus LMT site numbers are in bold, and BBMT-only site numbers are in normal type. First panel shows measured TM; second panel shows modeled TM; third panel shows measured TE; and fourth panel shows modeled TE.

combinations of starting models, regularization grids, data combinations, and minimizing/smoothing levels. Most of the inverse modeling was undertaken using the finite element inversion algorithm RLM2DI [*Mackie and Madden*, 1993; *Rodi and Mackie*, 2001], as implemented in the Geotools MT interpretation software package. This inversion code was found to be very stable and capable of reducing the model misfit to acceptable levels. The rapid relaxation inversion (RRI) algorithm [*Smith and Booker*, 1991; *Wu et al.*, 1993] was also used in order to compare and test model parameter resolution. Both inversion algorithms search iteratively for the smoothest models that fit the observed data while minimizing simultaneously the horizontal and vertical resistivity gradients between cells. Thus the final models obtained represent the models with least structure in them; models with more structure are acceptable and will fit the data equally well, but models with less structure would not fit the data. Topography was not considered as the area of study is essentially flat at regional scales. Local topography is too small-scale given the site spacing.

[36] The best fit RLM2DI model is illustrated in Figure 6 for the crustal section; all of the main features in the model (labeled A–E) also appear in the RRI model (not shown, see *Solon* [2000]). Models that are more complex than these are possible, but any less complexity results in an unacceptable misfit between the model and the data.

[37] Both the model illustrated in Figure 6 and the RRI model were derived from fitting the TM and TE mode apparent resistivities and phases simultaneously. Nine of the 21 modeled MT stations were combined BBMT + LMT sites (Figure 3), which typically contributed data from 40 periods to the inversion. The remaining 12 sites were BBMT-only sites (Figure 3) and contributed up to 30 periods to the inversions. The periods modeled ranged from 0.004 s to 14,285 s (>7 decades), with highest quality, therefore higher weight, in the period range of 1–1000 s corresponding to midcrustal depths (10–30 km). Many of the sites had scattered data points with extremely large error bars at the longest periods: these data were deemed unreliable and were not used in the inversions.

[38] Inversions using several different starting models were tested; a uniform half-space, two-layer, three-layer, and basic block configurations. Most of the separate starting model inversions resulted in final models with the same first-order electrical structures. However, those beginning from a homogenous, 100 Ω m half-space resulted in the smoothest models with the best fit for both inversions. The final RLM2DI and RRI inversions were derived with an impedance noise floor of 5% (equivalent to 10% in apparent resistivity and 2.8° in phase) in order to reset unrealistically small error estimates that may lead to overly emphasized structure. After 76 iterations the RLM2DI model (Figure 6), with 84 columns and 41 rows, misfit the observed data to within 10% overall and to within 8% at 16 of the 21 sites. Further iterations did not change the model in any significant manner. Most of the misfit is concentrated at data from a few sites, and was usually the result of the inability

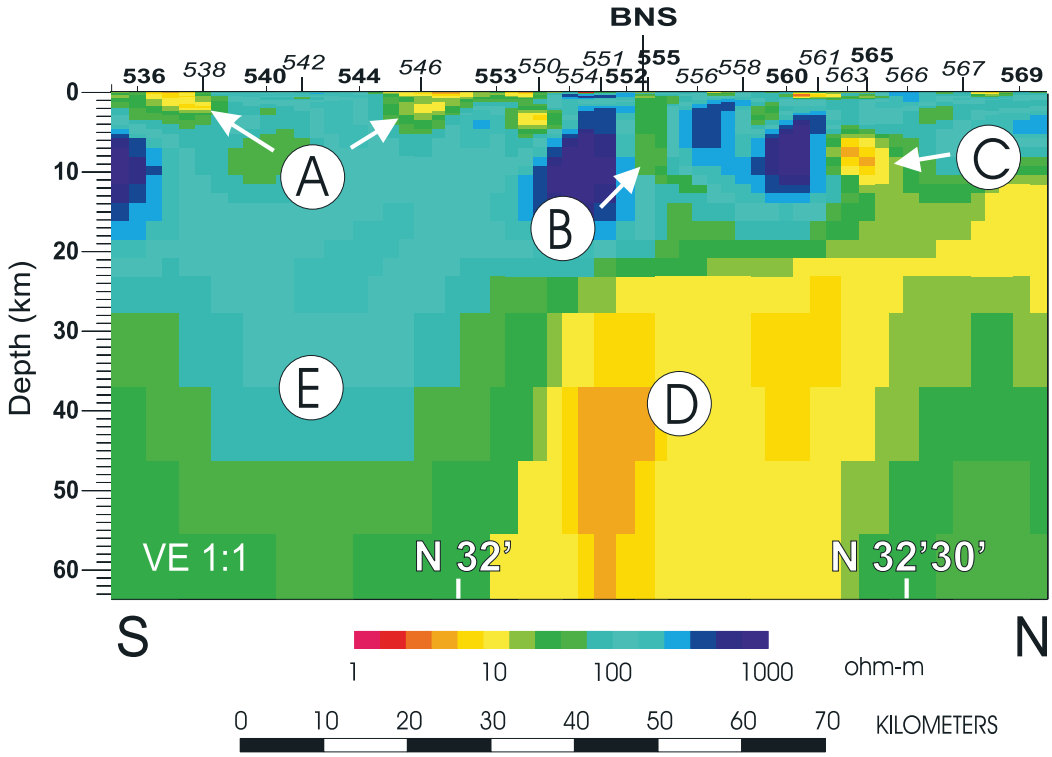

Figure 6. Resistivity model of the Banggong-Nujiang suture zone derived by RLM2DI. Hot colors (reds and yellows) indicate areas of low resistivity (or high conductivity), whereas cool colors (blues and purple) indicate zones of high resistivity (or low conductivity). Numbers at the top represent the individual site locations. Letters represent model features discussed in the text. BBMT plus LMT site numbers are in bold, and BBMT-only site numbers are in normal type.

of the inversion algorithms to fit the TE mode apparent resistivity data at long periods. The two inversion strategies resulted in similar electrical geometries of the suture zone subsurface; however, because of the better fit to the observed data with RLM2DI compared to RRI, discussion will refer to the RLM2DI model unless otherwise noted.

[39] A qualitative comparison of the fit of the modeled response to the observed estimates can be made by examining the apparent resistivity and phase pseudosections plotted in Figure 5. In addition, the differences in phase between the final inverse model and the acquired data were calculated and the pseudosections for each mode are shown in Figure 7. For the majority of data points the fit is generally good and between ±2° in phase. Also, the misfit pseudosections (Figure 7) do not exhibit regions of systematic misfit caused by correlated residuals, indicating that there is no major structural feature that is sensed by the data but is not present in the model of Figure 6. Taken together, the large number of data points being modeled, the satisfactory overall misfit of the model to the observed data, and the fact that the resultant electrical geometries of both inversion strategies are nearly equivalent, all suggest that the first-order electrical features apparent in both models are robust.

6.2. The 500 Line Resistivity Model Features

[40] In general, the crust beneath the profile is anomalously conductive compared to other intracontinental regions [e.g., *Jones*, 1992]. Resistivities in the upper crust are typically in the high hundreds to thousands of ohm meter range, and drop to tens of ohm meters with increasing depth at all sites across the profile. These observations are consistent with the predominately low-resistivity crust sensed across the entire Tibetan Plateau from the Himalaya to the Kunlun Shan [*Wei et al.*, 2001] from longitudes of approximately 90°E in the south to 95°E in the north.

[41] The transition from a resistive upper crust (>300 Ω m) to conductive middle to lower crust occurs at variable depth across the profile. It is thickest to the south beneath sites 538 to 546, where a pronounced resistive root extends to 40+ km depth (model feature E in Figure 6). From there, the base of the resistive layer shallows rapidly northward directly below the BNS zone to depths of 15–20 km beneath the northern half of the profile. The northward thinning of the resistive upper layer is paralleled by a northward decrease in the resistivity of the middle crust, which reaches its minimum value beneath stations 551 to 565 (model feature D in Figure 6). These first-order features are evident in both RLM2DI and RRI final models, though their forms are different due to the different spatial smoothing approaches used in the two algorithms. This rapid change in resistivity occurs at the same location as a dramatic change of seismic polarization anisotropy (Figure 3), from <0.5 s to the south to >1.5 s to the north [*Huang et al.*, 2000], and a subvertical, low-velocity anomaly to midcrustal (~30 km) depths [*Haines et al.*, 2003; *Mechie et al.*, 2004; *Meissner et al.*, 2004].

[42] Within the generally resistive upper crust, four small but prominent conductive features are observed. In the

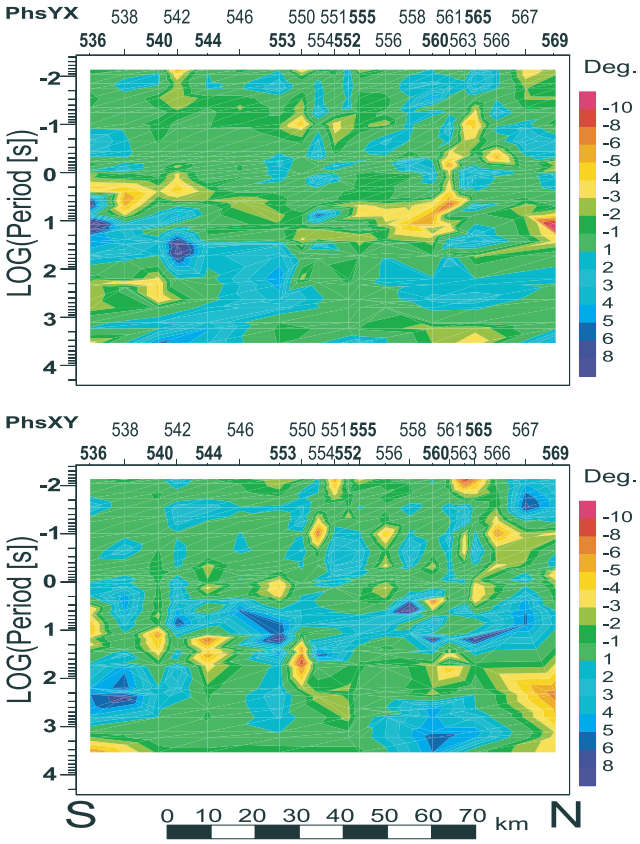

Figure 7. Pseudosections illustrating the misfit between the observed phase responses and the RLM2DI theoretical phase responses. BBMT plus LMT site numbers are in bold, and BBMT-only site numbers are in normal type. (top) TM phase misfit; and (bottom) TE phase misfit.

southern half of the profile, two zones of low resistivity (10–50 Ω m) extend from the surface to ~4 km in depth. These anomalies correlate spatially with the Cenozoic Duba and Lunpola sedimentary basins (features A in Figures 3 and 6), which are roughly E-W trending and merge just west of the profile. This broader basin we refer to as the Lunpola/Duba basin. Toward the middle of the profile, beneath site 555 just north of the surface trace of the BNS, a narrow conductive zone extends from the surface to the top of the conductive middle crust at ~20 km depth (feature B in Figures 3 and 6). This conductor is approximately coincident with, and slightly north of, an ENE-WSW trending left-lateral strike-slip fault zone, which has an obvious topographic expression and which coincides with the BNS at the longitude of the profile [*Kidd et al.*, 1988] (Figure 3). Hot springs and large associated tufa mounds are observed along the most prominent strand of this fault about 65 km ENE of the MT profile. Toward the northern end of the profile, a small but extremely conductive feature occurs at about 6 km depth beneath sites 563 and 565 (1–5 Ω m, feature C in Figures 3 and 6). This feature dips steeply toward the north in both the RLM2DI and RRI models, and may connect with the conductive middle crust at 15–20 km depth. This anomaly occurs in a wide NNE trending valley which contains Lake Doima (32.30°N, 89.10°E); hot springs are located at the western edge of the lake. This topographic feature is probably fault controlled and of largely extensional origin, although the valley margins are not now obvious active fault scarps. Model feature C is located to the north of the northernmost ophiolites, which defines the surface trace of the BNS. Whether feature B is north of the BNS or is collocated with the BNS and therefore caused by the faulting itself [*Taylor et al.*, 2003] requires a higher resolution MT study across the BNS with far smaller site spacing.

[43] A collocated wide-angle seismic reflection/refraction experiment conducted by INDEPTH indicates that refraction Moho beneath the profile is at 65 ± 5 km depth (see below) [*Zhao et al.*, 2001], and is observed to be a complex boundary [*Meissner et al.*, 2004]. To within error, reflection Moho is at the same depth, occurring at 22 s two-way travel time equivalent to depths of 62–65 km [*Ross et al.*, 2004]. Thus our final models show low-resistivity material apparently extending into the upper mantle (see below). Is low resistivity in the uppermost mantle required, or is it an artifact of the spatial smoothing used in the inversion algorithms? This question is of interest because of the possibility that mantle-derived melt may have been intruded into the crust in relatively recent time, and produced the observed southern high heat flow [*Francheteau et al.*, 1984] and overall high conductance [*Wei et al.*, 2001] of the Tibetan crust. The other end-member possibility is that the high heat flow and high conductivity (low resistivity) are entirely due to in situ melting and/or metamorphic dewatering of the thickened Tibetan crust, caused by radiogenic heating. If melt is traversing the uppermost mantle beneath the survey, one might expect the resistivity of the uppermost mantle to be several orders of magnitude lower than if it is dry [*Ledo and Jones*, 2005].

[44] The resistivity of the upper mantle in stable continental regions has generally been difficult to measure, due to the existence of relatively conductive lower crust in most regions (<100 Ω m) [*Jones*, 1999]. The resistivity of the oceanic uppermost mantle has been measured using a large-scale controlled-source experiment, and found to be on the order of 100,000 Ω m [*Cox et al.*, 1986], consistent with a dry peridotite composition, but a similar controlled-source experiment would be impractical on the continents. Recent MT experiments in the Archean Slave and Rae provinces of Canada, which are unusual in lacking a conductive lower crust, have shown upper mantle resistivity values of ~4000 Ω m [*Jones and Ferguson*, 2001] and >40,000 Ω m [*Jones et al.*, 2002] for the Slave and Rae province, respectively. The electromagnetic shielding effect of the thick conductive middle and lower crust in Tibet has made estimation of the resistivity of the upper mantle difficult. *Unsworth et al.* [2004] present evidence for a relatively conductive upper mantle beneath northern Tibet, and *Spratt et al.* [2005] tentatively conclude, from a single site north of the Zangbo suture in southern Tibet, that the Indian mantle plate is resistive.

7. Resistivity Model Appraisal

[45] To test how sensitive features of our final RLM2DI model (Figure 6) are to the MT data, a wide range of

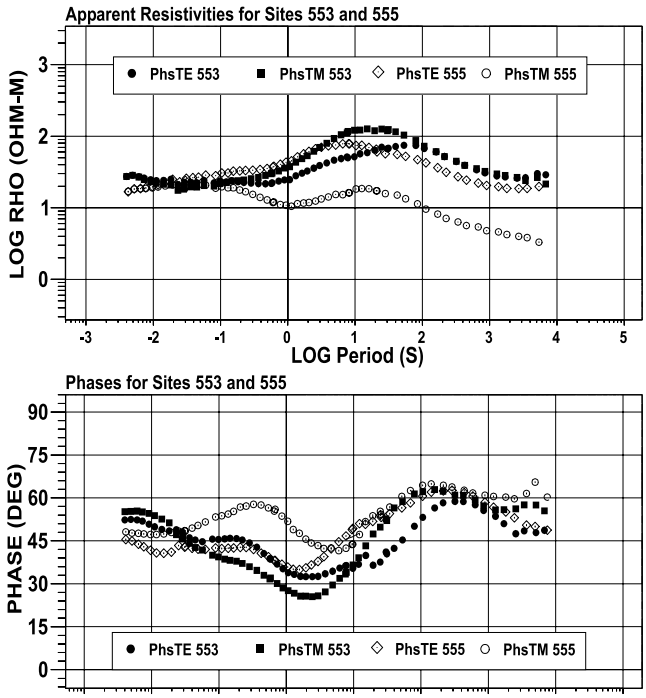

Figure 8. (top) Apparent resistivity and (bottom) phase curves for sites 553 (solid circles, TE; squares, TM) and 555 (open diamonds, TE; circles, TM).

representative resistivity models were constructed and their responses computed using the PW2D finite element forward modeling code of *Wannamaker et al.* [1984]. Because of the sensitivity of apparent resistivities to near surface effects, and the possibility that there are remnant unresolved static shift factors, the TM and TE phases were examined preferentially over their corresponding apparent resistivities. The phase misfits between the final inversion model responses and altered model responses were computed; this allows for assessment of the sensitivity of the data to particular features of the final model.

7.1. Middle and Lower Crustal Resistivity Variations

[46] A prominent feature of the final model is the south-to-north variation in the resistivity of the middle and lower crust across the profile. Resistivity values of ~100 Ω m are modeled at ~40 km depth beneath the southern part of the profile (resistive root, feature E in Figure 6), diminishing to ~40 Ω m at greater depth. In contrast, resistivity values of 4 Ω m to 25 Ω m occur in the same depth range on the northern half of the model (feature D in Figure 6). The transition between the two regions is relatively sharp and steep in both the RLM2DI and RRI final models, and occurs below the surface trace of the BNS, as defined by the northern limit of ophiolite fragments. Figure 8 shows the TM and TE apparent resistivity and phase curves from sites 553 and 555, located south and north of the BNS, respectively. (Note that errors are not shown on Figure 6 to enhance clarity. Data errors were typically less than the model error floors of 10% in apparent resistivity and 2.8° in phase, or about the size of the symbols.) The apparent resistivity and phase responses for the TE data are similar for both sites, but the TM data show substantial differences at virtually all periods. The TM data from site 553, south of the transition, shows a moderately resistive upper and middle crust, with gradually decreasing resistivity at periods corresponding to lower crustal depths. Site 555, just to the north of the surface trace of the suture, exhibits low resistivity values at all periods, implying a significant difference in the crustal resistivity structure beneath the two sites. The question is, how sensitive are these MT data to variations in resistivity in the middle to deep crust?

[47] First, we examine the area of moderate resistivity in the midcrust and lower crust at the north end of the profile beneath sites 566, 567 and 569 (north of feature D, Figure 6). The modeled resistivity of this region is 20–50 Ω m, which is approximately half an order of magnitude more resistive than the area of lower resistivity immediately to the south beneath sites 554 to 565. Is this slightly more resistive zone required by the data or is it an artifact of effects off the end of the profile in the inversion process? The resistivity of the zone was changed to 10 Ω m to match the resistivities for model feature D (Figure 6), and the forward responses were computed and compared to the final model responses and the observed data. The TE phase differences (not shown) show little sensitivity to the change, suggesting that the TE data are insensitive to either resistivity structure. Conversely, the TM phases show a misfit of 6°–7° at the longest periods, whereas the original model fit the observed data to within 2° in phase (Figure 5). For site 569 at the longest periods the altered model does not fit the observed or modeled data. In particular, the altered model misfits the drop in phase (increase in apparent resistivity) from periods of ~500 s to ~5000 s. These observations indicate that this area of the model fits the observed data better with a more resistive body at middle and lower crust depths.

[48] The next sensitivity test involved changing the area of lowest resistivity in the middle and lower crust (model feature D; beneath sites 550–561) to more resistive values (Figure 9). The middle section of the model, originally ≤10 Ω m, was changed to 25 Ω m, equal to that further north. The phase misfit differences between the modified model responses and the original model responses range from 3° to 6° at periods ≥20 s. The data most sensitive to change is in the TM mode below sites 556 to 561, where the misfit was 5°–6° in phase at periods of ~100 s. The RLM2DI model fits the data to within 1–2° at these sites and periods (Figures 5 and 7). Figure 10 illustrates the observed, modeled, and forward modeled TM mode data from sites 560 and 556, which are both vertically above the region of the model most affected by the changes made to the RLM2DI model. At periods between 50 s and 1000 s the calculated forward responses of the altered model do not fit the observed or modeled data, missing the relatively large increase in phase (decrease in apparent resistivity) at those periods. Increasing the resistivity of the same general area of the model (to 160 Ω m) resulted in large misfits (>10°) in both modes for nearly the entire lateral extent of the data. These tests demonstrate that a model with less resistive material in the middle crust of the central part of the profile fits the data better than the modified, more resistive structure. This is particularly true beneath sites

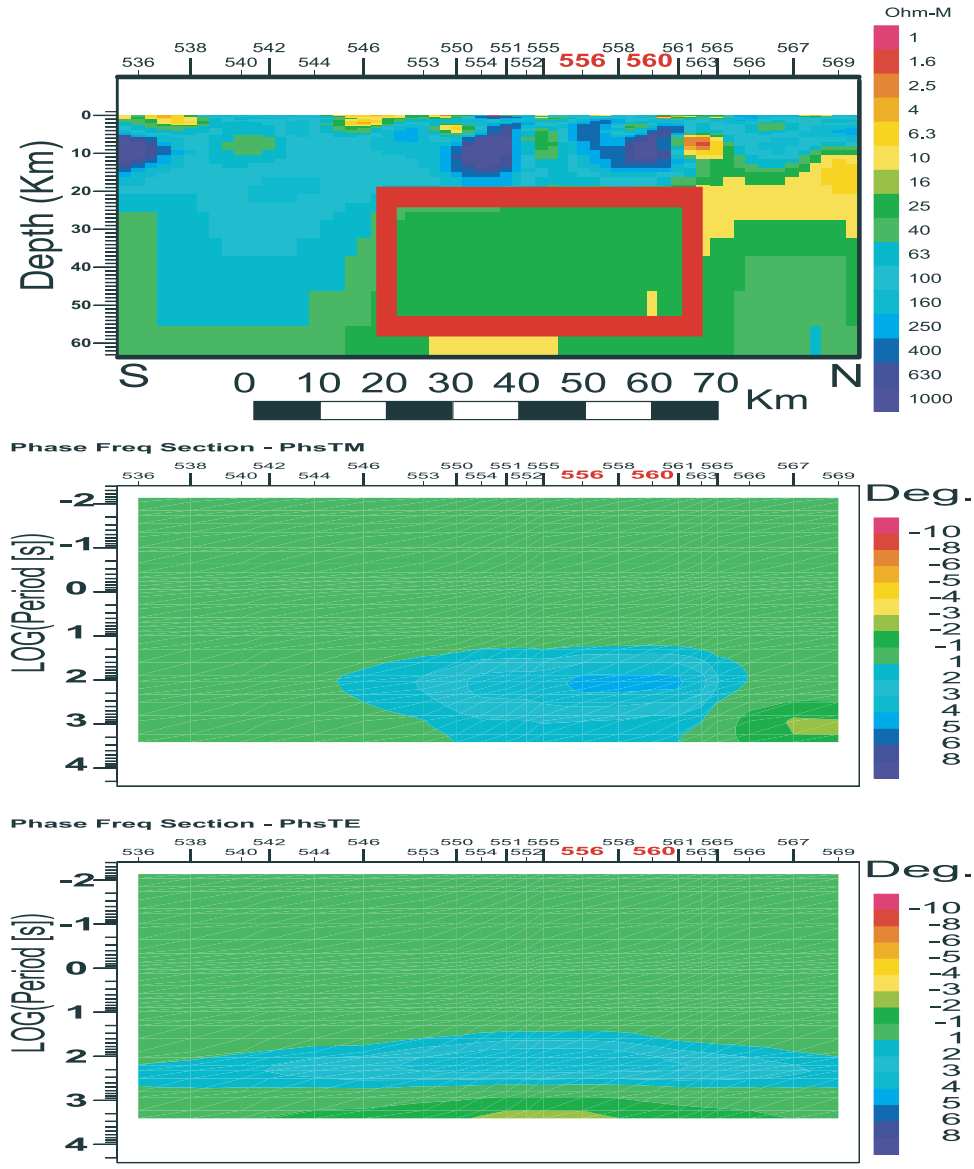

Figure 9. (top) Altered 2-D model. (middle) TM mode forward phase response difference. (bottom) TE mode forward phase response difference. Red box highlights area of alteration.

556 to 561, where the misfit of the modified structure is greatest.

7.2. Upper Crustal Resistivity Variations

[49] Both the final RLM2DI (Figure 6) and RRI models show four zones of anomalously low resistivity in the upper crust (model features A, B, and C on Figure 6). How robust are these model features and what constraints do they add?

[50] The Cenozoic Duba and Lunpola subbasins are both imaged as relatively low-resistivity (5–10 Ω m) anomalies at the surface (model features A in Figures 3 and 6), as expected of young sedimentary basins. The direct correlation of these model features to mapped basin geology, both in lateral extent and estimated depth (~4 km), serves as good parameter control for both inversions.

[51] To test data sensitivity to model features B and C (Figure 3 and 6), the zones were changed to more resistive values (250 Ω m) that more closely approximate the background resistivity of the uppermost crust. The phase differences between the forward responses of the altered model and the original model are nearly 10° for sites above both of the modified regions. The final RLM2DI model fit the data at the sites coincident with model feature B to within 2°–3° in both modes, and model feature C to less than 5° in both modes. The observed TM data, the inversion model TM responses, and the forward model TM responses from the modified model from sites 555 and 565 are plotted in Figure 11. These two sites are the BBMT + LMT sites above the region of the model most affected by the changes to the two regions of low resistivity. The plots illustrate that at periods between 0.01 s and 10 s the calculated forward responses of the altered model are clearly different from the observed or modeled data. These observations suggest that conductive features B and C in

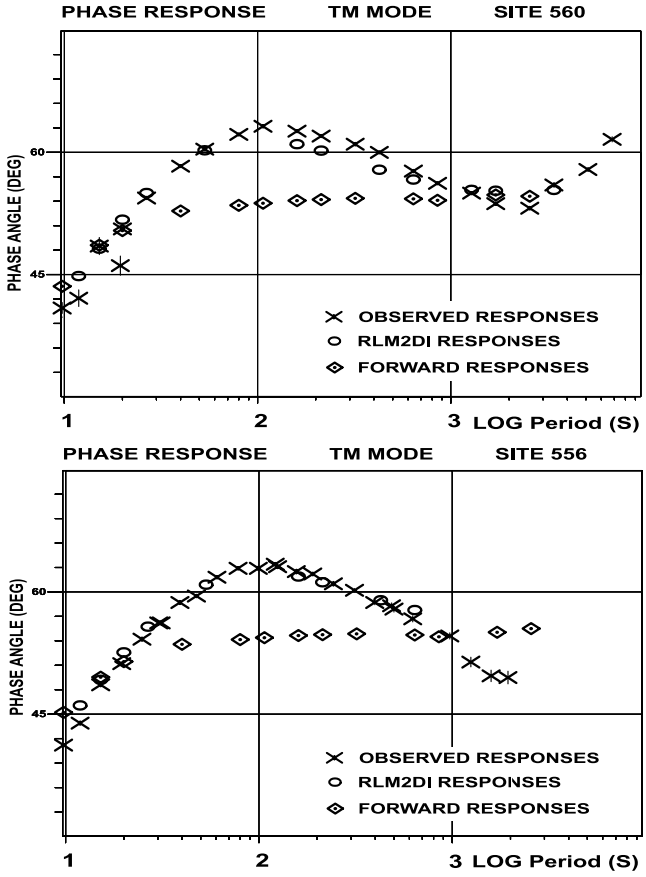

Figure 10. Observed TM mode responses (crosses), the TM model responses from the RLM2DI inversion model (Figure 6, circles), and the TM forward modeled responses from the altered model (Figure 9, top, diamonds) for sites (top) 560 and (bottom) 556.

the upper crust are robust model features that are required by the data.

7.3. Upper Mantle Resistivity

[52] A series of model tests was conducted to determine whether the 500 line MT data provide any constraints on the resistivity of the uppermost mantle beneath Tibet in this region. We derived the maximum depth of sensitivity by placing an electrically resistive (1000 Ω m) basement (half-space) at various depths and then computing the forward responses. The top of the resistive basement was initially placed at 150 km depth, and shallowed by 20 km increments to 70 km. The forward responses show virtually no sensitivity to resistive basement when it is at 150 km, and only the longest two periods from site 544 are sensitive to the basement when placed at 130 km. The phase response differences of the longest periods from the southern LMT sites (536–553) exceeds the errors of the observed data when the resistive basement is placed at a depth of 110 km, but the northern sites are not sensitive to the basement at this depth. The phase difference of the final inversion is exceeded across the entire profile when the resistive basement is placed at 90 km. The same exercise was performed with a conductive (5 Ω m) basement and essentially the same results were observed. Not surprisingly, the data in the southern part of the profile, where the conductance of the overlying crust is lowest, sense to greater depth because of the lesser crustal shielding of the EM waves. This difference is due to the presence of the more conducting middle and lower crust to the north of the BNS, compared to the south, that attenuates the EM fields thereby limiting penetration.

[53] To further constrain the depth of sensitivity of our model to the data, the inductive response function (C(w, k)) [*Schmucker*, 1970; *Jones*, 1980] was determined at each LMT site across the profile from the TE impedance data. This method uses the longest measured period of the apparent resistivity, and the phase angle at that period, to estimate the depth to which the 1-D MT fields have penetrated using *Weidelt*'s [1972] depth of maximum eddy current flow concept. Estimates of depth of penetration range from a minimum of 50 km below site 560 at the northern end of the profile, to a maximum depth of 190 km below site 544 at the southern end of the profile (Figure 12). As with the forward model test, there appears to be a significant difference in depth sensitivity between the four southern LMT sites (536, 540, 544, 553) and the five northern LMT ones (552, 555, 560, 565, 569). The mean of the estimated depth of penetration for the four southern LMT sites is 135 km, compared to 75 km for the northern sites. Taking the minimum estimates from the LMT sites,

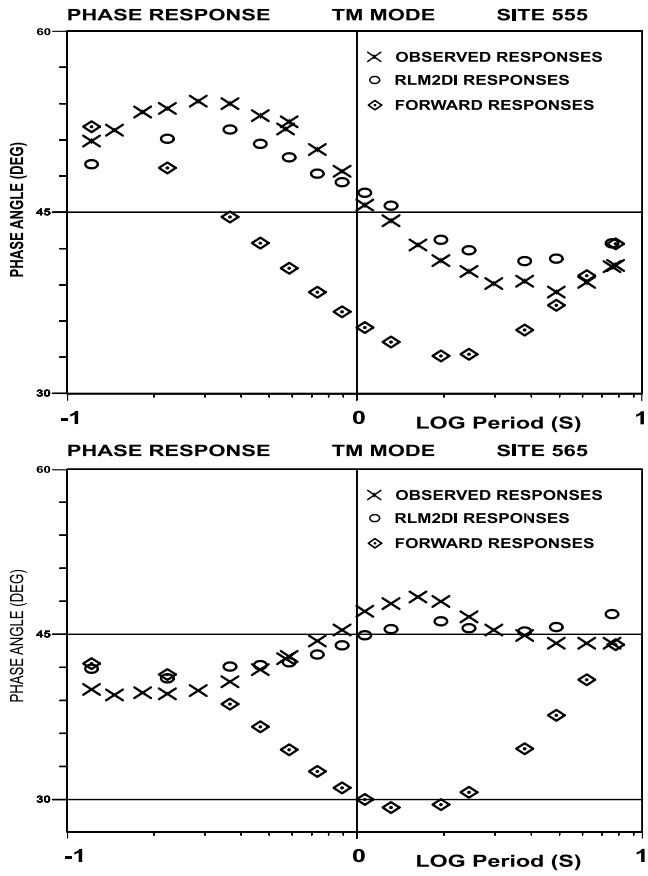

Figure 11. Observed TM mode responses (crosses), the TM model responses from the RLM2DI inversion model (Figure 6, circles), and the TM forward modeled responses from an altered model excluding features B and C in Figure 6 (diamonds) for sites (top) 555 and (bottom) 565.

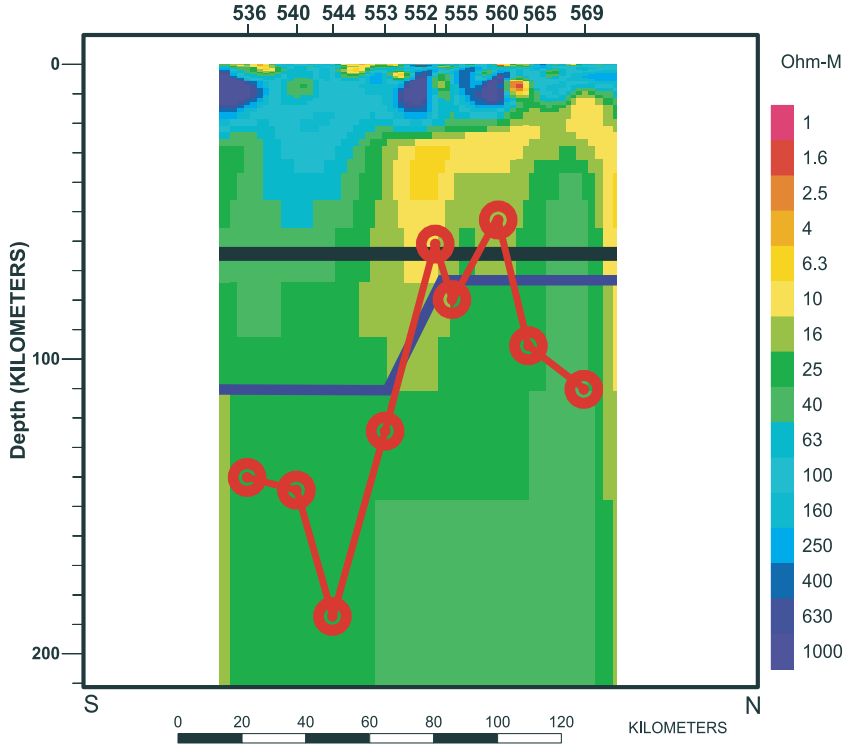

Figure 12. Depth of penetration for the BBMT plus LMT sites as estimated from the real part of the inductive response function ($C(w, k)$) [*Schmucher*, 1970; *Jones*, 1980]. Calculated depths are illustrated by red dots. Blue line represents estimated depth of penetration from forward sensitivity testing. For reference, the estimated depth (65 ± 5 km) of the Moho is illustrated by the black line.

these sensitivity tests suggest that the data are sensing to about 110 km in the south and about 75 km depth in the north of the BNS.

[54] The inferences that the southern LMT data are sensitive to resistivity below the Moho raises the question of whether the final models adequately resolve any deep resistivity variations that might exist, particularly the existence of a resistive lithospheric lid. Visual inspection of the apparent resistivity responses shows no evidence for an increase of resistivity at periods correlating to Moho and greater depths. However, the TM phases from every LMT site across the profile shows a slight decrease in phase beginning at ~200 seconds s. This drop of 3°–7° in phase is then followed by increasing phase at periods of 1000 s to 5000 s to the longest periods measured (Figure 13). These observations of the TM phase responses suggest that there may be an increase in the resistivity at approximately Moho depth, which is not represented in the final models.

[55] In order to test the possibility of a resistive mantle lid beneath our profile, a resistive layer at Moho depths overlying a conductive asthenosphere was thinned iteratively. The asthenosphere was assigned a model resistivity of 40 Ω m, broadly consistent with global values worldwide [see, e.g., *Jones*, 1999]. The top of the resistive mantle lid (Moho) corresponds to a period of approximately 200 s. Responses for models with an infinitely thick, 85 km thick and 45 km thick mantle lid misfit the phase data at the southern sites at periods >200 s. The 25 km thick mantle lid model misfits the southern site data, from 200 s to 1000 s, by about 4° in phase. A 10 km thick mantle lid is effectively undetectable. Taken together, these results are suggestive of a thin (less than or equal to a few tens of kilometers) or absent mantle lid, and hence shallow asthenosphere, beneath the profile. This result is necessarily tentative, but is consistent with the location of the profile near the southern edge of the region of northern Tibet characterized by low upper mantle seismic velocities and Neogene alkalic volcanism (discussed subsequently).

8. Comparison With Coincident Seismological Observations

[56] Several of the INDEPTH seismological studies in central Tibet have relevance to the interpretation of the MT data presented here. *Zhao et al.* [2001], *Haines et al.* [2003], *Mechie et al.* [2004], and *Meissner et al.* [2004] describe the results of the INDEPTH III wide-angle reflection experiment colocated on the 500 line MT profile. The portion of *Zhao et al.*'s [2001] crustal V_p model overlapping with our profile is shown on Figure 14. The *P* wave data recorded in this experiment define the Moho at 65 ± 5 km depth beneath the center of the profile, shallowing slightly to the north, and three crustal layers of laterally varying thickness distinguished on the basis of wide-angle reflections. The upper layer, immediately beneath the low-velocity near surface, ranges in velocity from about 5.6 to 6.2 km/s, the intermediate layer from about 6.0 to 6.5 km/s and the lower layer from about 6.5 to 7.3 km/s. Within the middle crust, *P* wave velocities decrease northward by ~0.2 to ~0.5 km/s where midcrustal resistivity also decreases substantially northward (Figure 14). This first-order correlation is consistent with our inference that the northward

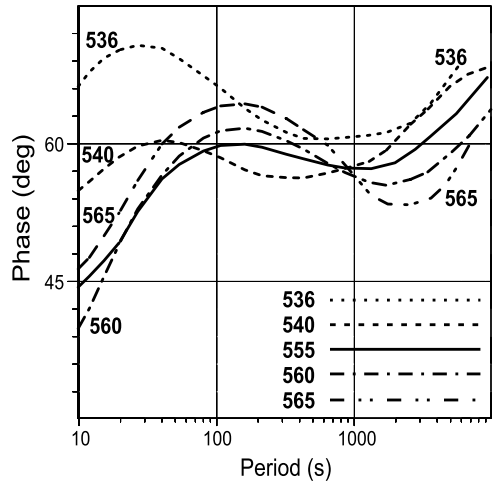

Figure 13. Long-period TM mode responses from several of the LMT sites across the profile. Decrease in phase of this mode seen at periods correlating to Moho depths, ~200 s and 65 km, respectively, is illustrated.

decrease in midcrustal resistivity is due to a local northward increase in the melt and/or fluid content of the middle crust. Beneath the northern part of the MT profile there is also a reasonable correspondence between the modeled depth to the top of the midcrustal velocity layer (15–20 km depth, wide-angle reflection Pi1P of *Zhao et al.* [2001]) and the top of the conductive middle crust.

[57] *Mechie et al.* [2004] present an *S* wave velocity and Poisson's ratio model from the INDEPTH wide-angle data. They infer from the seismological data, taken together with supporting evidence from the MT model, that they can map the alpha-beta quartz transition in the midcrust. North of the BNS it lies at about 18 km at a temperature of about 700°C, whereas south of the BNS it lies at 32 km depth with a temperature of 800°C.

[58] At shallow depths, the conductive Lunpola and Duba basins are clearly confined to the low-velocity surficial layer defined in the wide-angle experiment. There is a gross correlation between the region of lowest velocities sensed in the upper crustal layer (5.6–5.7 km/s) and the position of the BNS and nearby Cenozoic strike-slip faults. Analysis of short-offset seismic data acquired during shooting of the wide-angle profile confirms the existence of this local velocity minimum [*Haines et al.*, 2000, 2003]. The wide-angle reflection shot records indicate that wide-angle crustal refractions (phase *Pg*) from the southern shots were highly attenuated (missing?) in the offset range corresponding to the surface trace of the suture and nearby strike-slip faults. In contrast, *Pg* is strong at these locations on the northern (south looking shots) shot records. Our speculative interpretation is that the upper crust in the vicinity of the suture contains one or more narrow, steeply south dipping low-velocity channels. The *Pg* phase traveling northward is refracted down, producing a local shadow zone, whereas *Pg* traveling southward is refracted up and recorded. The average seismic velocity of the upper crustal region containing the channels would be low. The narrow steeply dipping low-resistivity features B and C (Figures 6 and 14) occur within the shadow zone and presumably are low-velocity channels, though their direction of dip is not resolvable from these regional MT data. The obvious geological interpretation is that the steep low-velocity low-resistivity channels are fractured fluid-filled fault zones of the Neogene transcurrent fault system localized along the BNS.

[59] *Huang et al.* [2000] have analyzed passive seismic data recorded on the INDEPTH III transect for seismic polarization anisotropy. The INDEPTH III passive array was the densest broadband passive seismic array so far deployed in Tibet, and the results are striking. *SKS* and *SKKS* phases from earthquakes in the Tonga-Fiji region and South America exhibit little resolvable splitting (<0.5 s) for stations south of ~32°N; conversely, stations north of 32°N exhibit substantial splitting (~2 s), with variable but generally east-west fast direction (Figure 3). The transition occurs at approximately the same location that the MT model shows the pronounced northward decrease in midcrustal resistivity (Figures 6 and 14). Seismic polarization anisotropy is generally considered to reflect a coherent strain fabric within the mantle lithosphere or underlying asthenosphere [e.g., *Silver and Chan*, 1991], although in some circumstances it might be largely or entirely produced within the crust (e.g., by crustal penetrating vertically oriented schists [*Okaya et al.*, 1995; *Godfrey et al.*, 2000]). Following *Holt* [2000], *Huang et al.* [2000] have interpreted the strong anisotropy beneath northern Tibet, north of the BNS, as reflecting distributed transcurrent shear within the underlying uppermost mantle related to the regional eastward tectonic escape of northern Tibet. They further suggested that the very sharp boundary of the anisotropic region at ~32°N marks the northern edge of

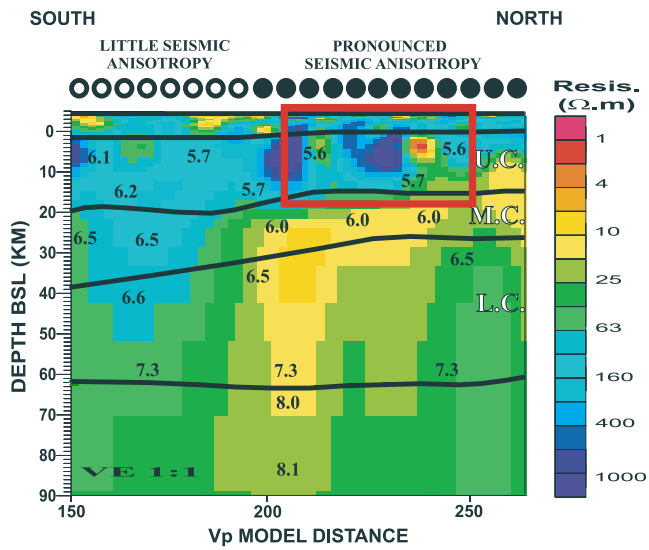

Figure 14. Overlay of V_p model crustal boundary layers and point V_p (taken from *Zhao et al.* [2001]) onto the final RLM2DI MT model (Figure 6). Note vertical scale has been modified from Figure 6 to depths with respect to sea level. Annotations refer to features described in text. U.C., V_p model upper crust; M.C., V_p model middle crust; L.C., V_p model lower crust. Red box outlines V_p model distances 200–245 km corresponding to an area of seismic attenuation described in text.

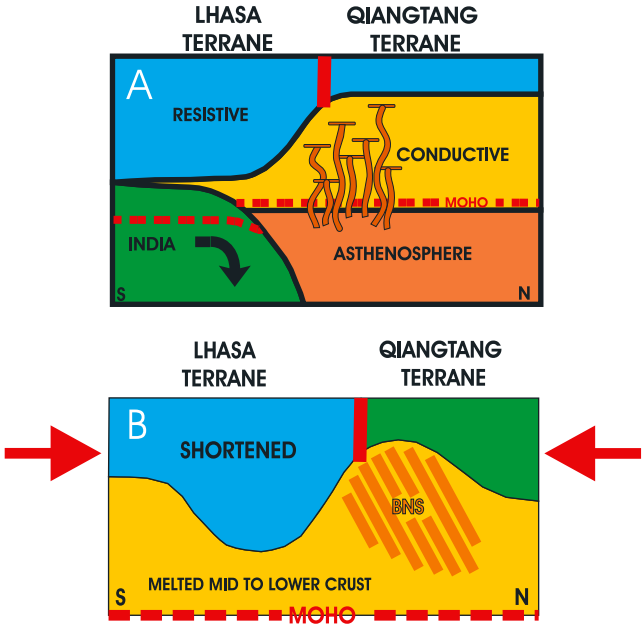

Figure 15. Cartoons illustrating two possible end-member models to explain the resistivities observed: (a) How the conductivity structure seen beneath the BNS zone may be controlled by the northward increase in the amount of mantle derived melt intruded into the middle and lower crust. (b) How the conductivity structure seen beneath the BNS zone may be controlled by preexisting geologic structure. In this hypothesis, the northern Lhasa Terrane has been shortened during the Cenozoic and resists anatexis, whereas the subduction zone complex rocks of the BNS are more easily melted.

underthrust Indian lithosphere (seismically isotropic), which bounds the actively deforming region to the north. *Meissner et al.* [2004] suggest a modified explanation of the anisotropy in terms of massive lithospheric escape of the Qiangtang block to the east.

9. Tectonic Interpretation

[60] Implicit in the *SKS* splitting interpretation is the concept that the actively deforming upper mantle beneath northern Tibet is thought to be hotter relative to that to the south [*Kind et al.*, 2002]. The low uppermost mantle seismic velocities and low Q in the north [*Owens and Zandt*, 1997], together with the occurrence of Neogene alkalic volcanics on the northern plateau [*Turner et al.*, 1993], further suggest that it contains at least some basaltic melt. This would imply a thin or nonexistent electrical lithosphere (resistive mantle lid) beneath the region, consistent with our tentative interpretation that the uppermost mantle beneath our MT profile is conductive. One interpretation is that the northward decrease in midcrustal resistivity evident on the MT profile is a manifestation of the edge of the hot deforming mantle region. For example, perhaps the intrusion of basaltic melt into the crust underlying the northern part of the profile enhances the melt fraction within the crust there in comparison to the south (see Figure 15a). Alternatively, *Hacker et al.* [2000] noted that lower crustal xenoliths in the volcanics can be interpreted in the context of dry partial melting of pelitic rocks of the lower crust without direct mantle involvement. Partially molten rocks are expected to exhibit low resistivity due to ionic conduction [e.g., *Schilling et al.*, 1997; *Partzsch et al.*, 2000].

[61] Given present knowledge, however, it is also possible that the midcrustal resistivity variations along the profile are entirely controlled by preexisting and/or evolving crustal structures. One such feature is the resistive root underlying the southern part of the profile at the northern edge of the Lhasa terrane, beneath the Lunpola/Duba basin. Along strike to the east, strata of equivalent age to the older parts of the Lunpola basin are deformed into a Tertiary thrust belt (Amdo thrust belt) with dominantly northward underthrusting [*Coward et al.*, 1988; *Kidd et al.*, 1988], and faults within the northern border of the Lunpola basin show evidence of the same largely north directed underthrusting deformation, some of it quite young (Pliocene [*Burke and Lucas*, 1989; *Kidd and Molnar*, 1988]). This is generally taken to reflect localized crustal shortening along the BNS (reactivation) related to the India-Asian collision, although the claim of southward directed underthrusting at this site [*Meyer et al.*, 1998; *Tapponnier et al.*, 2001] is not supported by the geological observations referenced above, nor by the geophysical data. Following our line of reasoning, the resistive root beneath the southern part of the MT profile might simply be the result of local shortening (thickening and/or northward underthrusting and consequent "refrigeration") of the resistive upper crust during the Cenozoic. Taking this a step further, the northern edge of the Lhasa terrane contains an extensive early mid-Cretaceous granitic batholith belt (Baingoin granites), which at depth is presumably refractory. When depressed (and heated) this material might be relatively resistant to remelting. In contrast, pelite-rich rock within the BNS immediately to the north, and under much of the Qiangtang terrane on the hypothesis of *Kapp et al.* [2000], would be expected to be comparatively fertile, and thus when heated should produce an electrically significant melt/fluid fraction (see Figure 15b). These speculations require further examination.

10. Summary

[62] INDEPTH MT data from a 150-km-long profile crossing the Banggong-Nujiang suture (BNS) in central Tibet have been processed and modeled in more detail than has been the case with previously published studies of MT data from Tibet. The results confirm that, to first order, the region is characterized by a resistive upper crust (hundreds to thousands of ohm meters) overlying an anomalously conductive middle to lower crust (approximately tens of ohm meters), as appears to be generally the case within the Tibetan Plateau [*Wei et al.*, 2001]. Viewed in detail, however, there are marked lateral and vertical variations in crustal resistivity beneath the region, which can be correlated with known surface geological features and compared with coincident seismological observations.

[63] Tensor decomposition analysis indicates that regional electrical structures in the crust are approximately two-dimensional with an approximately east-west geoelectric strike, similar to the surface geological strike in the region. The resistive upper crust varies from ~15 km to ~45 km in thickness. It is thickest beneath the southern part of the

profile where it defines a resistive root centered beneath the northern edge of the Lhasa terrane and superimposed Neogene Lunpola and Duba basins. Immediately to the north, the resistive upper crust thins and the middle crust becomes quite conductive (resistivity <10 Ω m). Coincident wide-angle seismic data indicate that this highly conductive region also has lower *P* wave velocity than the surrounding middle crust. The transition occurs close to the surface trace of the BNS, as defined by outcrops of Late Jurassic ophiolites, and is essentially coincident with a prominent active left-lateral fault which also locally forms the northern edge of the Lunpola basin. This fault is part of a system of Cenozoic transcurrent faults that extend east-west across central Tibet (Karakorum-Jiali fault system), and, at the longitude of the MT 500 line, is localized along the preexisting BNS. All of these crustal features additionally coincide with the locus of northward decreasing upper mantle seismic velocities and *Q* beneath Tibet (summarized by *Owens and Zandt* [1997]), and a dramatic northward increase in seismic polarization anisotropy [*Huang et al.*, 2000].

[64] As the anomalously low resistivity of the middle crust in Tibet is a ubiquitous phenomenon beneath our profiles which transect the whole plateau, we believe its proximal cause must be interconnected melt and/or aqueous fluids generated during the Tertiary collisional phase of the plateau's evolution [*Nelson et al.*, 1996; *Makovsky and Klemperer*, 1999; *Partzsch et al.*, 2000; *Wei et al.*, 2001]. In southern Tibet anatectic crustal melts and metamorphic brines generated as a consequence of crustal thickening are the most likely candidates. In northern Tibet, in addition to those, it is likely that mantle derived melts have been injected into the lower crust in relatively recent time [*Turner et al.*, 1993; *Owens and Zandt*, 1997; *Hacker et al.*, 2000]. Although the MT data analyzed here do not allow discrimination of the type(s) of fluid residing in the crust, they do indicate strong, local, structural control on its distribution. Not unexpectedly, discrete conductors in the upper crust clearly coincide with Neogene sedimentary basins, and Neogene to Recent transcurrent faults. In the middle crust, the region of the BNS is significantly more conductive, and by inference significantly more fluid rich, than the northern edge of the Lhasa terrane at the same depth immediately to the south. The nature of this structural control is, however, problematic. Is the BNS simply the southern limit of recent mantle derived magmatism in Tibet, or is it composed of more fertile material that has produced relatively more fluid/melt during Tertiary heating than the region to the south, or has the resistive upper crust to the south simply been thickened by Tertiary shortening? This question is not resolvable at present. Finally, our MT model hypothesis testing suggests that the resistivity of upper mantle beneath Tibet can be constrained, at least locally, despite the shielding effect of the anomalously conductive plateau crust. To date, this has only been done partially successfully in Tibet, in the north [*Unsworth et al.*, 2004] and from one site in the south [*Spratt et al.*, 2005], although the issue is of substantial tectonic significance. In the small area examined here, it appears that the electrical mantle lithosphere (electrically resistive mantle lid) is thin or nonexistent.

[65] **Acknowledgments.** K. Douglas Nelson passed away unexpectedly on 17 August 2002. Doug was a true visionary, who led the INDEPTH project with drive, insight, and humor. K.D.S. was the last graduate student to complete his thesis under Doug's supervision. We will all be forever grateful for having had the opportunity to cross Doug's path during our careers. We dedicate this paper to Doug's memory. The MT component of Project INDEPTH has been supported by the Ministry of Land and Natural Resources of China and the U.S. National Science Foundation's Continental Dynamics Program. Data acquisition along the profile was assisted by Brian Roberts (GSC) and Juanjo Ledo (University of Barcelona). We thank our INDEPTH colleagues for their input into this paper, particularly Larry Brown and Jim Mechie. An Yin, Pamela Lezaeta, and Associate Editor Steve Park provided substantial comments on the original version that have greatly improved our paper, and we are grateful to them for their attention to detail. Geological Survey of Canada contribution 2002225.

References

Agarwal, A. K., H. E. Poll, and J. T. Weaver (1993), One- and two-dimensional inversion of magnetotelluric data in continental regions, *Phys. Earth Planet. Inter.*, *81*, 155–176.

Alsdorf, D., and K. D. Nelson (1999), The Tibetan satellite magnetic low: Evidence for widespread melt in the Tibetan crust?, *Geology*, *27*, 943–946.

Andersen, F., D. B. Boerner, K. Harding, A. G. Jones, R. D. Kurtz, J. Parmelee, and D. Trigg (1988), LIMS: Long period intelligent magnetotelluric system, paper presented at 9th Workshop on EM Induction, Int. Assoc. of Geomagn. and Aeron., Sochi, Russia, 24–31 Oct.

Argand, E. (1924), La tectonique de l'Asie, *Int. Geol. Cong. Rep. Sess.*, *13*, 170–372.

Armijo, R., P. Tapponnier, J. L. Mercier, and T.-L. Han (1986), Quaternary extension in southern Tibet: Field observations and tectonic implications, *J. Geophys. Res.*, *91*, 13,803–13,872.

Armijo, R., P. Tapponnier, and T. Han (1989), Late Cenozoic right-lateral strike-slip faulting in southern Tibet, *J. Geophys. Res.*, *94*, 2787–2838.

Brown, L. D., W. Zhao, K. D. Nelson, M. Hauck, D. Alsdorf, A. Ross, M. Cogan, M. Clark, X. Liu, and J. Che (1996), Bright spots, structure, and magmatism in southern Tibet from INDEPTH seismic reflection profiling, *Science*, *274*, 1688–1690.

Burg, J.-P., F. Proust, P. Tapponnier, and G.-M. Chen (1983), Deformation phases and tectonic evolution of the Lhasa block (southern Tibet, China), *Eclogae Geol. Helv.*, *76*, 643–665.

Burke, K., and L. Lucas (1989), Thrusting on the Tibetan Plateau within the last 5 Ma, in *Tectonic Evolution of the Tethyan Region*, *NATO ASI Ser., Ser. C*, vol. 259, edited by A. Sengor et al., pp. 507–512, Springer, New York.

Camfield, P. A., and D. I. Gough (1977), A possible Proterozoic plate boundary in North America, *Can. J. Earth Sci.*, *14*, 1229–1238.

Chave, A. D., and A. G. Jones (1997), Electric and magnetic field distortion decomposition of BC87 data, *J. Geomagn. Geoelectr.*, *49*, 767–789.

Chen, L., J. R. Booker, A. G. Jones, N. Wu, M. L. Unsworth, W. Wei, and H. Tan (1996), Electrically conductive crust in southern Tibet from INDEPTH magnetotelluric surveying, *Science*, *274*, 1694–1996.

Coward, M. P., W. S. F. Kidd, P. Yun, R. M. Shackleton, and Z. Hu (1988), The structure of the 1985 Tibet Geotraverse, Lhasa to Golmud, *Philos. Trans. R. Soc. London, Ser. A*, *327*, 307–336.

Cox, C. S., S. C. Constable, A. D. Chave, and S. C. Webb (1986), Controlled-source electromagnetic sounding of the oceanic lithosphere, *Nature*, *320*, 52–54.

Dewey, J. F., and K. C. A. Burke (1973), Tibetan, Variscan, and Precambrian basement reactivation: Products of continental collision, *J. Geol.*, *81*, 683–692.

Dewey, J. F., R. M. Shackleton, C. Chengfa, and S. Yiyin (1988), The tectonic evolution of the Tibetan Plateau, *Philos. Trans. R. Soc. London, Ser. A*, *327*, 379–413.

Duba, A., S. Heikamp, W. Meurer, G. Nover, and G. Will (1994), Evidence from borehole samples for the role of accessory minerals in lower-crustal conductivity, *Nature*, *367*, 59–61.

Egbert, G. D. (1997), Robust multiple-station magnetotelluric data processing, *Geophys. J. Int.*, *130*, 475–496.

Evans, S., A. G. Jones, J. Spratt, and J. Katsube (2005), Central Baffin electromagnetic experiment (CBEX): Maping the North American Central Plains (NACP) conductivity anomaly in the Canadian arctic, *Phys. Earth Planet. Inter.*, *150*, 107–122.

Fielding, E. J., B. L. Isacks, M. Barazangi, and C. C. Duncan (1994), How flat is Tibet?, *Geology*, *22*, 163–167.

Francheteau, J., C. Jaupart, X. S. Shen, W.-H. Kang, D.-L. Lee, J.-C. Bai, H.-P. Wei, and H.-Y. Deng (1984), High heat flow in southern Tibet, *Nature*, *307*, 32–36.

Fuji-ta, K., T. Katsura, and Y. Tainosho (2004), Electrical conductivity measurement of granulite under mid- to lower crustal pressure-temperature conditions, *Geophys. J. Int.*, *157*, 79–86.

Gamble, T. D., W. M. Goubau, and J. Clarke (1979), Magnetotellurics with a remote reference, *Geophysics*, *44*, 53–68.
Girardeau, J., J. Marcoux, C. J. Allègre, J. P. Bassoullet, Y. Tang, X. Xiao, Y. Zao, and X. Wang (1984), Tectonic environment and geodynamic significance of the Neo-Cimmerian Donqiao ophiolite, Bangong-Nujiang suture zone, Tibet, *Nature*, *307*, 27–31.
Godfrey, N. J., N. I. Christensen, and D. A. Okaya (2000), Anisotropy of schists: Contributions of crustal anisotropy to active-source seismic experiments and shear wave splitting observations, *J. Geophys. Res.*, *105*, 27,991–28,007.
Groom, R. W., and R. C. Bailey (1989), Decomposition of magnetotelluric impedance tensors in the presence of local three-dimensional galvanic distortion, *J. Geophys. Res.*, *94*, 1913–1925.
Groom, R. W., R. D. Kurtz, A. G. Jones, and D. E. Boerner (1993), A quantitative methodology for determining the dimensionality of conductive structure from magnetotelluric data, *Geophys. J. Int.*, *115*, 1095–1118.
Hacker, B. R., E. Gnos, L. Ratschbacher, M. Grove, M. McWilliams, S. V. Sobolev, J. Wan, and Z. Wu (2000), Hot and dry deep crustal xenoliths from Tibet, *Science*, *287*, 2463–2466.
Haines, S. S., S. L. Klemperer, J. Mechie, L. Brown, K. D. Nelson, A. Ross, Z. Wenjin, and G. Jingru (2000), Upper crustal structure of central Tibet revealed through velocity modeling, *Eos Trans. AGU*, *81*(48), Fall Meet. Suppl., Abstract T52B-03.
Haines, S. S., S. L. Klemperer, L. Brown, G. Jingru, J. Mechie, R. Meissner, A. Ross, and Z. Wenjin (2003), INDEPTH III seismic data: From surface observations to deep crustal processes in Tibet, *Tectonics*, *22*(1), 1001, doi:10.1029/2001TC001305.
Harris, N. B. W., R. Xu, C. L. Lewis, and C. Jin (1988), Plutonic rocks of the 1985 Tibet Geotraverse: Lhasa to Golmud, *Philos. Trans. R. Soc. London, Ser. A*, *327*, 145–168.
Harris, N. B. W., S. Inger, and R. Xu (1990), Cretaceous plutonism in central Tibet; an example of post-collision magmatism?, *J. Volcanol. Geothermal Res.*, *44*, 21–32.
Harrison, T. M., P. Copeland, W. S. F. Kidd, and O. Lovera (1995), Activation of the Nyainqentanghla shear zone: Implications for uplift of the southern Tibetan Plateau, *Tectonics*, *14*, 658–676.
Hennig, A. (1915), Zur petrographie und geologie von sudwest-Tibet, in *Southern Tibet*, vol. 5, edited by S. Hedin, 220 pp., Lithogr. Inst., Swed. Army, Norstedt, Stockholm.
Hochstein, M., and K. Regenauer-Lieb (1998), Heat generation associated with collision two plates: The Himalayan geothermal belt, *J. Volcanol. Geotherm. Res.*, *83*, 75–92.
Holt, W. (2000), Correlated crust and mantle strain fields in Tibet, *Geology*, *28*, 67–70.
Huang, W. C., et al. (2000), Seismic polarization anisotropy beneath central Tibetan Plateau, *J. Geophys. Res.*, *105*, 27,979–27,989.
Jiracek, G. R. (1990), Near-surface and topographic distortions in electromagnetic induction, *Surv. Geophys.*, *11*, 163–203.
Jiracek, G. R., V. Haak, and K. H. Olsen (1995), Practical magnetotellurics in a continental rift environment, in *Continental Rifts: Evolution, Structure, Tectonics*, edited by K. H. Olsen, pp. 103–129, Elsevier, New York.
Jones, A. G. (1980), Geomagnetic induction studies in Scandinavia: I - Determination of the inductive response function from the magnetometer data, *J. Geophys.*, *48*, 181–194.
Jones, A. G. (1988), Static shift of magnetotelluric data and its removal in a sedimentary basin environment, *Geophysics*, *53*, 967–978.
Jones, A. G. (1992), Electrical conductivity of the continental lower crust, in *Continental Lower Crust*, edited by D. M. Fountain, R. J. Arculus, and R. W. Kay, pp. 81–143, Elsevier, New York.
Jones, A. G. (1993a), Electromagnetic images of modern and ancient subduction zones, *Tectonophysics*, *219*, 29–45.
Jones, A. G. (1993b), The COPROD2 dataset: Tectonic setting, recorded MT data and comparison of models, *J. Geomagn. Geoelectr.*, *45*, 933–955.
Jones, A. G. (1998), Waves of the future: Superior inferences from collocated seismic and electromagnetic experiments, *Tectonophysics*, *286*, 273–298.
Jones, A. G. (1999), Imaging the continental upper mantle using electromagnetic methods, *Lithos*, *48*, 57–80.
Jones, A. G., and I. Dumas (1993), Electromagnetic images of a volcanic zone, *Phys. Earth Planet. Inter.*, *81*, 289–314.
Jones, A. G., and I. J. Ferguson (2001), The electric Moho, *Nature*, *409*, 331–333.
Jones, A. G., and R. W. Groom (1993), Strike angle determination from the magnetotelluric tensor in the presence of noise and local distortion: Rotate at your peril!, *Geophys. J. Int.*, *113*, 524–534.
Jones, A. G., and H. Jödicke (1984), Magnetotelluric transfer function estimation improvement by a coherence-based rejection technique, paper presented at 1984 Annual SEG Meeting, Atlanta, Ga.
Jones, A. G., A. D. Chave, G. Egbert, D. Auld, and K. Bahr (1989), A comparison of techniques for magnetotelluric response function estimates, *J. Geophys. Res.*, *94*, 14,201–14,213.
Jones, A. G., R. D. Kurtz, D. E. Boerner, J. A. Craven, G. McNeice, D. I. Gough, J. M. DeLaurier, and R. G. Ellis (1992), Electromagnetic constraints on strike-slip fault geometry—The Fraser River fault system, *Geology*, *20*, 561–564.
Jones, A. G., J. A. Craven, G. A. McNeice, I. J. Ferguson, T. Boyce, C. Farquharson, and R. G. Ellis (1993), The North American Central Plains conductivity anomaly within the Trans-Hudson orogen in northern Saskatchewan, *Geology*, *21*, 1027–1030.
Jones, A. G., J. Katsube, and P. Schwann (1997), The longest conductivity anomaly in the world explained: Sulphides in fold hinges causing very high electrical anisotropy, *J. Geomagn. Geoelectr.*, *49*, 1619–1629.
Jones, A. G., D. Snyder, S. Hanmer, I. Asudeh, D. White, D. Eaton, and G. Clarke (2002), Magnetotelluric and teleseismic study across the Snowbird Tectonic Zone, Canadian Shield: A Neoarchean mantle suture?, *Geophys. Res. Lett.*, *29*(17), 1829, doi:10.1029/2002GL015359.
Jones, A. G., J. Ledo, and I. J. Ferguson (2005), Electromagnetic images of the Trans-Hudson orogen: The North American Central Plains anomaly revealed, *Can. J. Earth Sci.*, *42*, 457–478.
Kapp, P., et al. (1998), Post-mid-Cretaceous shortening along the Banggong-Nujiang suture and in west-central Qiangtang, Tibet, *Eos Trans. AGU*, *79*, 794.
Kapp, P., M. A. Murphy, A. Yin, and L. Ding (1999), Cenozoic shortening along the Banggong-Nujiang suture zone, central Tibet, *Terra Nostra Abstr.*, *6*, 81–83.
Kapp, P., A. Yin, C. E. Manning, M. Murphy, T. M. Harrison, M. Spurlin, L. Ding, X. Deng, and C.-M. Wu (2000), Blueschist-bearing metamorphic core complexes in the Qiangtang Block reveal deep crustal structure of northern Tibet, *Geology*, *28*, 19–22.
Kariya, K. A., and T. J. Shankland (1983), Electrical conductivity of dry lower crustal rocks, *Geophysics*, *48*, 52–61.
Kidd, W. S. F., and P. Molnar (1988), Quaternary and active faulting observed on the 1985 Academia Sinica-Royal Society Geotraverse of Tibet, *Philos. Trans. R. Soc. London, Ser. A*, *327*, 337–363.
Kidd, W. S. F., Y. Pan, C. Chang, M. P. Coward, J. F. Dewey, F. R. S. A. Gansser, P. Molnar, R. M. Shackleton, and Y. Sun (1988), Geological mapping of the 1985 Chinese-British Tibetan (Xizang-Qinghai) Plateau Geotraverse route, *Philos. Trans. R. Soc. London, Ser. A*, *327*, 287–305.
Kind, R., X. Yuan, J. Saul, D. Nelson, S. V. Sobolev, J. Mechie, W. Zhao, G. Kosarev, J. Ni, U. Achauer, and M. Jiang (2002), Seismic images crust and upper mantle beneath Tibet: Evidence for Eurasian plate subduction, *Science*, *298*, 1219–1221.
Ledo, J., and A. G. Jones (2001), Regional electrical resistivity structure of the southern Canadian Cordillera and its physical interpretation, *J. Geophys. Res.*, *106*, 30,775–30,769.
Ledo, J., and A. G. Jones (2005), Temperature of the upper mantel beneath the Intermontane Belt, northern Canadian Cordillera, determined from combining mineral composition, electrical conductivity laboratory studies and magnetotelluric field observations, *Earth Planet. Sci. Lett.*, *236*, 258–268.
Ledo, J., A. G. Jones, and I. J. Ferguson (2002), Electromagnetic images of a strike-slip fault: The Tintina fault—Northern Canadian, *Geophys. Res. Lett.*, *29*(8), 1225, doi:10.1029/2001GL013408.
Leeder, M. R., A. B. Smith, and J. Yin (1988), Sedimentology, palaeoecology and palaeoenvironmental evolution of the 1985 Lhasa to Golmud Geotraverse, *Philos. Trans. R. Soc. London, Ser. A*, *327*, 107–143.
Li, S., M. J. Unsworth, J. R. Booker, W. Wei, H. Tan, and A. G. Jones (2003), Partial melt or aqueous fluid in the mid-crust of southern Tibet? Constraints from INDEPTH magnetotelluric data, *Geophys. J. Int.*, *153*, 289–304.
Mackie, R. L., and T. R. Madden (1993), Three-dimensional magnetotelluric inversion using conjugate gradients, *Geophys. J. Int.*, *115*, 215–229.
Makovsky, Y., and S. L. Klemperer (1999), Measuring the seismic properties of Tibetan bright spots: Evidence for free aqueous fluids in the Tibetan middle crust, *J. Geophys. Res.*, *104*, 10,795–10,825.
Marquis, G., A. G. Jones, and R. D. Hyndman (1995), Coincident conductive and reflective lower crust across a thermal boundary in southern British Columbia, Canada, *Geophys. Res.*, *96*, 12,259–12,291.
Martinez-Garcia, M. (1992), Electromagnetic induction in geothermal fields and volcanic belts, *Surv. Geophys.*, *13*, 409–434.
McNeice, G. W., and A. G. Jones (2001), Multi-site, Multi-frequency tensor decomposition of magnetotelluric data, *Geophysics*, *66*, 158–173.
Mechie, J., S. V. Sobolev, L. Ratschbacher, A. Y. Babeyko, G. Bock, A. G. Jones, K. D. Nelson, K. D. Solon, L. D. Brown, and W. Zhao (2004), Precise temperature estimation in the Tibetan crust from seismic detection of the alpha-beta quartz transition, *Geology*, *32*, 601–604.

Meissner, R., F. Tilmann, and S. Haines (2004), About the lithospheric structure of central Tibet, based on seismic data from the INDEPTH III profile, *Tectonophysics*, *380*, 1–25.

Meyer, B., P. Tapponnier, L. Bourjot, F. Metivier, Y. Gaudemer, G. Peltzer, S. Guo, and Z. Chen (1998), Crustal thickening in Gansu-Qinghai, lithospheric mantle subduction, and oblique, strike-slip controlled growth of the Tibet Plateau, *Geophys. J. Int.*, *135*, 1–47.

Minarik, W. G., and E. B. Watson (1995), Interconnectivity of carbonate melt at low melt fraction, *Earth Planet. Sci. Lett.*, *133*, 423–437.

Molnar, P. (1988), A review of the geophysical constraints on the deep structure of the Tibetan Plateau, the Himalaya and the Karakoram, and their tectonic implications, *Philos. Trans. R. Soc. London, Ser. A*, *326*, 33–88.

Murphy, M. A., A. Yin, T. M. Harrison, S. B. Durr, Z. Chen, F. J. Ryerson, W. S. F. Kidd, X. Wang, and X. Zhou (1997), Did the Indo-Asian collision alone create the Tibetan Plateau?, *Geology*, *25*, 719–722.

Narod, B. B., and J. R. Bennest (1990), Ring-core fluxgate magnetometers for use as observatory variometers, *Phys. Earth Planet. Inter.*, *59*, 23–28.

Nelson, K. D., et al. (1996), Partially molten middle crust beneath southern Tibet: Synthesis of project INDEPTH results, *Science*, *274*, 1684–1688.

Ni, J., and M. Barazangi (1983), High-frequency seismic wave propagation beneath the Indian Shield, Himalayan Arc, Tibetan Plateau and surrounding regions: High uppermost mantle velocities and efficient Sn propagation beneath Tibet, *Geophys. J. R. Astron. Soc.*, *72*, 665–689.

Norin, E. (1946), Geological explorations in western Tibet: Reports from the scientific expedition to the northwestern provinces of China under the leadership of Dr. Sven Hedin, *Publ. 29* (III), *Geology 7*, 205 pp., Tryckeri Aktiebolaget, Thule, Stockholm.

Okaya, D. N. Christensen, D. Stanley, and T. Stern (1995), Crustal anisotropy in the vicinity of the Alpine Fault Zone, South Island, New Zealand, *N. Z. J. Geol. Geophys.*, *38*, 579–583.

Olhoeft, G. R. (1981), Electrical properties of granite with implications for the lower crust, *J. Geophys. Res.*, *86*, 931–936.

Owens, T. J., and G. Zandt (1997), Implications of crustal property variations for models of Tibetan Plateau evolution, *Nature*, *387*, 37–43.

Pan, Y., and W. S. F. Kidd (1992), The Nyainqentanglha shear zone: A late Miocene extensional detachment in the southern Tibetan Plateau, *Geology*, *20*, 775–778.

Pan, Y., and W. S. F. Kidd (1999), Shortening in the southern Lhasa block during India-Asia collision. In: 14th Himalaya-Karakorum-Tibet Workshop Abstracts, *Terra Nostra*, *99*(2), 111–112.

Partzsch, G. M., F. R. Schilling, and J. Arndt (2000), The influence of partial melting on the electrical behavior of crustal rocks: Laboratory examinations, model calculations and geological interpretations, *Tectonophysics*, *317*, 189–203.

Pearce, J. A., and W. Deng (1988), The ophiolites of the Tibetan geotraverses, Lhasa to Golmud (1985) and Lhasa to Kathmandu (1986), *Philos. Trans. R. Soc. London, Ser. A.*, *327*, 215–238.

Pous, J., G. Munoz, W. Heise, J.-C. Melgarejo, and C. Quesada (2004), Electromagnetic imaging of Variscan crustal structures in SW Iberia: The role of interconnected graphite, *Earth Planet. Sci. Lett.*, *217*, 435–450.

Ritter, O., T. Ryberg, U. Weckmann, A. Hoffmann-Rothe, A. Abueladas, Z. Garfunkel, and DESERT Research Group (2003), Geophysical images of the Dead Sea Transform in Jordan reveal an impermeable barrier for fluid flow, *Geophys. Res. Lett.*, *30*(14), 1741, doi:10.1029/2003GL017541.

Rodi, W., and R. L. Mackie (2001), Nonlinear conjugate gradients algorithm for 2-D magnetotelluric inversion, *Geophysics*, *66*, 174–187.

Ross, A. R., L. D. Brown, P. Pananont, K. D. Nelson, S. Klemperer, Seth Haines, W. Zhao, and J. Guo (2004), Deep reflection surveying in central Tibet: Lower-crustal layering and crustal flow, *Geophys. J. Int.*, *156*, 115–128, doi:10.1111/j.1365-246X.2004.02119.x.

Rowley, D. B. (1996), Age of collision between India and Asia: A review of the stratigraphic data, *Earth Planet. Sci. Lett.*, *145*, 1–13.

Schilling, F. R., G. M. Partzsch, H. Brasse, and G. Schwarz (1997), Partial melting below the magmatic arc in the central Andes deduced from geoelectromagnetic field experiments and laboratory data, *Phys. Earth Planet. Inter.*, *103*, 17–31.

Schmucker, U. (1970), Anomalies of Geomagnetic variations in the south western United States, *Bull. Scripps Inst. Oceanogr.*, *13*, 1–165.

Shankland, T. J., and M. E. Ander (1983), Electrical conductivity, temperatures, and fluids in the lower crust, *J. Geophys. Res.*, *88*, 9475–9484.

Silver, P. G., and W. Chan (1991), Shear wave splitting and mantle deformation, *J. Geophys. Res.*, *96*, 16,429–16,454.

Smith, J. T., and J. R. Booker (1991), Rapid inversion of two and three-dimensional magnetotelluric data, *J. Geophys. Res.*, *96*, 3905–3922.

Solon, K. (2000), Electromagnetic images of the Banggong-Nujiang suture zone of central Tibet from INDEPTH-III magnetotelluric data, M.Sc. thesis, Syracuse Univ., Syracuse, N. Y., Dec.

Spratt, J. E., A. G. Jones, K. D. Nelson, M. J. Unsworth, and the INDEPTH MT Team (2005), Very long period magnetotelluric data across the India-Asia collision zone, *Phys. Earth Planet. Inter.*, *150*, 227–237.

Stanely, W. D., V. F. Labson, W. J. Nokleberg, B. Csejtey, and M. A. Fisher (1990), The Denali fault system and Alaska Range of Alaska: Evidence for underplated Mesozoic flysch from magnetotelluric surveys, *Geol. Soc. Am. Bull.*, *102*, 160–173.

Sternberg, B. K., J. C. Washburne, and L. Pellerin (1988), Correction for the static shift in magnetotellurics using transient electromagnetic soundings, *Geophysics*, *53*, 1459–1468.

Tapponnier, P., J. Mercier, R. Armijo, T. Han, and J. Zhou (1981), Field evidence for active normal faulting in Tibet, *Nature*, *294*, 410–414.

Tapponnier, P., Z. Xu, F. Roger, B. Meyer, N. Arnaud, G. Wittlinger, and J. Yang (2001), Oblique stepwide rise and growth of the Tibetan Plateau, *Science*, *294*, 1671–1677.

Taylor, M. H., A. Yin, P. Kapp, F. Ryerson, L. Ding, S. He, and Y. Zhou (2001), Coeval north-south shortening and east-west extension in central Tibet, *Eos Trans. AGU*, *82*(47), Fall Meet. Suppl., Abstract T12F-04.

Taylor, M., G. Peltzer, A. Yin, F. Ryerson, R. Finkel, and L. Ding (2002), Active deformation in central Tibet: Constraints from InSAR and geologic observations, *Eos Trans. AGU*, *83*(47), Fall Meet. Suppl., Abstract T51B-1153.

Taylor, M., A. Yin, F. J. Ryerson, P. Kapp, and L. Ding (2003), Conjugate strike-slip faulting along the Bangong-Nujiang suture zone accommodates coeval east-west extension and north-south shortening in the interior of the Tibetan Plateau, *Tectonics*, *22*(4), 1044, doi:10.1029/2002TC001361.

Turner, S., C. Hawkesworth, J. Liu, N. Rogers, S. Kelley, and P. van Calsteren (1993), Timing of Tibetan uplift constrained by analysis of volcanic rocks, *Nature*, *364*, 50–54.

Unsworth, M. L., P. E. Malin, G. D. Egbert, and J. R. Booker (1997), Internal structure of the San Andreas fault at Parkfield, California, *Geology*, *25*, 359–362.

Unsworth, M., W. Wenbo, A. G. Jones, S. Li, P. Bedrosian, J. Booker, J. Sheng, D. Ming, and T. Handong (2004), Crustal and upper mantle structure of northern Tibet imaged with magnetotelluric data, *J. Geophys. Res.*, *109*, B02403, doi:10.1029/2002JB002305.

van Ngoc, P., P. Boyer, X. C. Therme, L. Li, and G. Y. Yin (1986), Partial melting zones in the crust of southern Tibet from magnetotelluric results, *Nature*, *319*, 310–314.

Vozoff, K. (1972), The magnetotelluric method in the exploration of sedimentary basins, *Geophysics*, *37*, 98–141.

Vozoff, K. (Ed.) (1986), *Magnetotelluric Methods*, Soc. of Explor. Geophys., Tulsa, Okla.

Vozoff, K. (1991), The magnetotelluric method, in *Electromagnetic Methods in Applied Geophysics: Applications*, pp. 641–712, Soc. of Explor. Geophys., Tulsa, Okla.

Wannamaker, P. E., G. W. Hohmann, and S. H. Ward (1984), Magnetotelluric responses of three-dimensional bodies in layered earths, *Geophysics*, *49*, 1517–1533.

Wannamaker, P. E., W. M. Doerner, J. A. Stodt, and J. M. Johnson (1997a), Subdued state of tectonism of the Great Basin interior relative to its eastern margin based on deep resistivity structure, *Earth Planet. Sci. Lett.*, *150*, 41–53.

Wannamaker, P. E., J. M. Johnson, J. A. Stodt, and J. R. Booker (1997b), Anatomy of the southern Cordilleran hingeline, Utah and Nevada, from deep electrical resistivity profiling, *Geophysics*, *62*, 1069–1086.

Watanabe, T., and K. Kurita (1993), The relationship between electrical conductivity and melt fraction in a partially molten simple system: Archie's law behavior, *Phys. Earth Planet. Inter.*, *78*, 9–17.

Wei, W., et al. (2001), Widespread fluids in the Tibetan crust, *Science*, *292*, 716–718.

Weidelt, P. (1972), The inverse problem of geomagnetic induction, *Z. Geophys.*, *38*, 257–289.

Wu, N., J. R. Booker, and J. T. Smith (1993), Rapid two-dimensional inversion of COPROD2 data, *J. Geomagn. Geoelectr.*, *45*, 1073–1087.

Wu, X., I. J. Ferguson, and A. G. Jones (2002), Magnetotelluric response and geoelectric structure of the Great Slave Lake shear zone, *Earth Planet. Sci. Lett.*, *196*, 35–50.

Yin, A. (2000), Mode of Cenozoic east-west extension in Tibet suggesting a common origin of rifts in Asia during the Indo-Asian collision, *J. Geophys. Res.*, *105*, 21,745–21,759.

Yin, A., and T. M. Harrison (2000), Geologic evolution of the Himalayan-Tibetan orogen, *Annu. Rev. Earth Planet. Sci.*, *28*, 211–280.

Yin, A., P. A. Kapp, M. A. Murphy, C. E. Manning, T. M. Harrison, M. Grove, D. Lin, X.-G. Deng, and C.-M. Wu (1999), Significant late Neogene east-west extension in northern Tibet, *Geology*, *27*, 787–790.

Zhang, S., S. Wei, J. Wang, and X. Zhang (1996), Magnetotelluric sounding in the Qiangtang basin of Xizang (Tibet), *J. China Univ. Geosci.*, *21*, 198–202.

Zhao, W., K. D. Nelson, and Project INDEPTH Team (1993), Deep seismic reflection evidence for continental underthrusting beneath southern Tibet, *Nature*, *366*, 557–559.

Zhao, W., et al. (2001), Crustal structure of central Tibet as derived from project INDEPTH wide-angle seismic data, *Geophys, J. Inter.*, *145*, 486–498.

P. Bedrosian, U.S. Geological Survey, Crustal Imaging and Characterization Team, MS 964, Box 25046, Denver, CO 80225-0046, USA.

J. R. Booker and S. Li, Department of Earth and Space Sciences, University of Washington, Box 351310, Seattle, WA 98195, USA.

M. Deng, S. Jin, H. Tan, and W. Wei, China University of Geosciences Beijing, 29 Xueyuan Road, Beijing 100083, China.

A. G. Jones, Dublin Institute for Advanced Studies, 5 Merrion Square, Dublin 2, Ireland. (alan@cp.dias.ie)

W. F. Kidd, Department of Earth and Atmospheric Sciences, State University of New York, Albany, NY 12222-0001, USA.

K. D. Solon, Exxon Mobil, Exploration Company, 233 Benmar St. GP3-348, Houston, TX 77060, USA.

M. J. Unsworth, Department of Physics, Avadh Bhatia Physics Laboratory, University of Alberta, Edmonton, AB, Canada T6G 2J1.